

1
2
3
4
5
6
7
8
9
10
11
12
13
14
15
16
17

CHARACTERIZATION OF FLOCS AND FLOC SIZE
DISTRIBUTIONS USING IMAGE ANALYSIS

A Thesis

Presented to the Faculty of the Graduate School

of Cornell University

in Partial Fulfillment of the Requirements for the Degree of

Master of Science

by

Siwei Sun

February 2016

18

19

20

21

22

23

©2016 Siwei Sun

24

25

26

27

28

29

30

31

ABSTRACT

32

33 A nonintrusive digital imaging process was developed to study particle size distributions created
34 through flocculation and sedimentation. This process was calibrated by measuring standardized
35 polystyrene particles of known size and was utilized to count and measure individual kaolin clay
36 particles as well as aggregates formed by coagulation with polyaluminum chloride and
37 flocculation. Identification of out-of focus flocs was automated with LabVIEW and used to
38 remove them from the database that was analyzed. The particle diameter of the test suspension of
39 kaolinite clay was measured to be $7.7\pm 3.8\ \mu\text{m}$ and a linear relationship was obtained between
40 turbidity and the concentration of clay particles determined by imaging. The analysis technique
41 was applied to characterize flocs and floc particle size distribution as a function of coagulant
42 dose. Removal of flocs by sedimentation was characterized by imaging and the negative
43 logarithm of the fraction of turbidity remaining after settling had a positive linear association
44 with the logarithm of aluminum dose. The maximum floc size observed in the settled water was
45 less than $120\ \mu\text{m}$, which was in accordance with the value predicted by a terminal velocity model
46 for the capture velocity of the experimental tube settler of $0.21\ \text{mm/s}$.

47

48

49

BIOGRAPHICAL SKETCH

50

51 Siwei Sun was born in Shanghai, China in 1990. She graduated with a degree in Environmental
52 Science and Engineering from Shanghai Jiao Tong University in 2013. In college, she was a
53 member of a student group BLUE SKY and worked to enhance public environment
54 consciousness. Her experiences in the environmental field include a half-year internship in Toray
55 Advanced Materials Research Laboratories (China) and a two-year lab research on membranes
56 with Dr. Lina Chi. In September 2013, she entered Cornell University and started her study
57 towards the M.S. Degree in Environmental Engineering.

58

59

60

61

62

63

64

65

66

ACKNOWLEDGMENTS

67

68 This thesis is the product of the efforts of many people. First, I would like to thank Dr. Monroe
69 Weber-Shirk and Dr. Len Lion for their guidance and encouragement in the research. Their
70 support was critical to my work. I acknowledge the inspirational instruction of Dr. Monroe
71 Weber-Shirk. He has spent considerable time teaching me about the process of research inquiry.
72 I must also thank Dr. Len Lion for guiding the research with his practical advice. I would also
73 like to thank Dr. Damian Helbling who served as the minor advisor in the committee.

74 I am grateful to Casey Garland, William Pennock and Hui Zhi, three graduate students in the lab
75 who helped me with the project. I am also grateful to my friends and family. Words cannot
76 express the gratitude for their tremendous love and support.

77 Special thanks to Tim Brock, Cameron Willkens and Paul Charles who found solutions to
78 technical problems with the experimental apparatus.

79 I would also like to thank the U.S. National Science Foundation under Award Number 1437961
80 for their support of the research.

81

82

TABLE OF CONTENTS

84	BIOGRAPHICAL SKETCH	iii
85	ACKNOWLEDGMENTS	iv
86	TABLE OF CONTENTS.....	v
87	LIST OF FIGURES	vii
88	LIST OF TABLES	x
89	LIST OF ABBREVIATIONS.....	xi
90	LIST OF SYMBOLS	xii
91	CHAPTER 1: INTRODUCTION.....	1
92	CHAPTER 2: CHARACTERIZATION OF FLOCS AND FLOC SIZE DISTRIBUTION	3
93	2.1 Abstract	3
94	2.2 Introduction	4
95	2.3 Experimental Methods	6
96	2.3.1 Flocculator Setup.....	6
97	2.3.2 Imaging system.....	8
98	2.4 Image analysis	12
99	2.4.1 Identification of particles.....	12

100	2.4.2 Removing out-of focus particles.....	15
101	2.5 Terminal velocity	21
102	2.6 Results.....	24
103	2.6.1 Validation of image analysis method	24
104	2.6.2 Effect of coagulant dose	29
105	2.6.3 Comparison between flocculated water and settled water.....	35
106	2.7 Conclusions	37
107	2.8 Future work	39
108	2.9 References	40
109	APPENDIX.....	44
110	A. Calculation of G , Q , L	44
111	B. Flow rate, coagulant dose and influent turbidity	47
112	C. Tube settler	47
113	D. Number concentration of primary particles.....	49
114	E. Fractal dimension.....	52
115	REFERENCES.....	58
116		
117		

LIST OF FIGURES

119	Figure 1. Schematic of the experimental apparatus.	7
120	Figure 2. Imaging system consisting of LED light, CCD camera attached to a computer and the	
121	suspended sample in a flow cell.	8
122	Figure 3. Airy disks. (A) Airy pattern and intensity distribution. (B) Airy patterns around a	
123	particle.	9
124	Figure 4. Application of local thresholding. (A) The original image with flocs. (B) Local	
125	thresholding applied to image A.	13
126	Figure 5. Example of morphological transformation. (A) Original grey scale image, (B) image	
127	after background correction and closing objects, (C) image after filling holes, (D) image after	
128	removing small particles or particles that touched the border of the image.	14
129	Figure 6. Sample image of identified and measured flocs.	17
130	Figure 7. Sample image of identified and measured flocs.	18
131	Figure 8. Flowchart of image analysis procedure.	20
132	Figure 9. Terminal velocity versus floc diameter.	22
133	Figure 10. pC^* versus floc size.	23
134	Figure 11. Image of standardized 3 μm polystyrene particles taken by the camera setup.	25
135	Figure 12. Schematic of experimental set up for image analysis method verification.	26

136 Figure 13. Average diameter of clay particles at different turbidities. 27

137 Figure 14. Number of clay particles per sample volume versus turbidity. 29

138 Figure 15. pC* versus PACL dose (mg/L as Al). 30

139 Figure 16. Floc size distributions of settled water according to different bin sizes (PACl dose =

140 0.53 mg/L as Al). 31

141 Figure 17. Log-log plot of floc size distributions of settled water according to different bin sizes

142 (PACl dose = 0.53 mg/L as Al). 32

143 Figure 18. Floc size distributions of settled water at different PACl dose (mg/L as Al). 33

144 Figure 19. Floc number concentration in the settled water versus PACl dose (mg/L as Al). 34

145 Figure 20. Size distributions of flocculated water and settled water at different PACl doses (mg/L

146 as Al). (TS designates tube settler.) 35

147 Figure 21. pC* value versus floc size. 37

148 Figure 22. Tube settler. 48

149 Figure 23. Estimated number of primary particles in the effluent at different aluminum doses

150 based on an assumed fractal dimension of 2.3. Solid line is fit of number of particles per NTU

151 based on Figure 14. 50

152 Figure 24. Primary particle distribution in the settled water at different PACL dose (mg/L as Al).

153 51

154 Figure 25. Primary particle distribution of flocculated water and settled water at different PACl

155 doses (mg/L as Al). (TS designates tube settler.) 52

156 Figure 26. Sample images of flocs..... 54

157 Figure 27. The regression of the logarithm of floc diameter vs. the logarithm of primary particle

158 numbers..... 55

159 Figure 28. Volume fractal dimension of flocs. 57

160

161

162

163

164

165

166

167

168

169

170
171
172
173
174
175
176
177
178
179
180
181
182
183
184
185
186

LIST OF TABLES

Table 1. Identified flocs in Figure 6 with their associated α and β values. Bold values meet the constraints. 18

Table 2. Identified flocs in Figure 7 with their associated α and β values. Bold values meet the constraints. 19

Table 3. Mean and standard deviation for 3.0 μm standardized particles 25

Table 4. Exponential fit and power law fit in Figure 19..... 35

LIST OF ABBREVIATIONS

187

188 I the matrix of the original image pixel values

189 I_f the sobel filter of the image matrix

190 NTU Nephelometric Turbidity Unit

191 PACl Polyaluminum chloride

192 ROI Region of interest

193 SSE sum of squared errors of prediction

194

195

196

197

198

199

200

201

202

203

LIST OF SYMBOLS

204	$A_{flowcell}$	cross sectional area of the flow cell (L^2)
205	A_{pixel}	projected area of particles in pixels
206	A_{tube}	cross sectional area of flocculator tube (L^2)
207	C_{Al}	Al concentration of coagulant stock (M/L^3)
208	C_{clay}	clay concentration added to raw water (M/L^3)
209	$C_{effluent}$	fraction of the effluent turbidity caused by the floc size class
210	$C_{influent}$	fraction of the influent turbidity caused by the floc size class
211	C_{plant}	Al dose within the flocculator (M/L^3)
212	D	inner diameter of the flocculator tube (L)
213	$D_{fractal}$	3-D fractal dimension
214	D_p	2D fractal dimension
215	D_v	3D fractal dimension described by Maggi and Winterwerp
216	d	floc diameter (L)
217	d_{clay}	diameter of primary particle (L)

218	d_{pixel}	spherical-equivalent diameter in pixels
219	G	velocity gradient (1/t)
220	$G_{CampStein}$	velocity gradient described by Camp and Stein (1/t)
221	\bar{G}	average velocity gradient (1/t)
222	\bar{G}_c	average velocity gradient in figure eight flocculator (1/t)
223	$\overline{G_{Gregory}}$	velocity gradient described by Gregory (1/t)
224	H_{image}	depth of field (L)
225	k	total floc number
226	L_{image}	height of the image (L)
227	L_{tube}	length of the flocculator tube (L)
228	$L_{tube settler}$	length of tube settler (L)
229	l	length scale of the sobel filter kernel (L)
230	l_{pixel}	pixel size (L)
231	NA	numerical aperture
232	n_0	number of primary particles counted in a 2D image
233	n_i	number of primary particle in floc i
234	n_{total}	total number of primary particles within sample volume

235	P	power input ($M \cdot L^2/t^3$)
236	P_{pixel}	perimeter of flocs (in pixels)
237	$pC *$	removal efficiency
238	Q_{Al}	flow rate of coagulant solution (L^3/t)
239	$Q_{flowcell}$	flow rate in flow cell (L^3/t)
240	Q_{plant}	flow rate of the plant (L^3/t)
241	R	radius of the pipe (L)
242	R_c	diameter of curvature of the flocculator coils (L)
243	r	radial distance from the pipe axis (L)
244	S	inner width of the tube settler (L)
245	t	operation time (t)
246	V	volume of the pipe (L^3)
247	V_{clay}	clay volume measured according to the images (L^3)
248	v_0	the maximum velocity in the fluid
249	$v_{capture}$	capture velocity of tube settler (L/t)
250	v_r	velocity of fluid at a radial distance r from the pipe axis (L/t)
251	v_t	floc terminal velocity (L/t)

252	$v_{tube\ settler}$	velocity inside tube settler (L/t)
253	v_{up}	vertical component of the velocity in the tube settler (L/t)
254	\bar{v}	average velocity of fluid (L/t)
255	W_{image}	width of the image (L)
256	x	dimensionless floc size
257	α	normalized minimum pixel value
258	α_t	threshold value of normalized pixel value
259	β	dimensionless maximum floc image intensity gradient
260	β_t	threshold value of image intensity gradient
261	Δp	pressure drop along the pipe [M/(L·t ²)]
262	ε	average energy dissipation rate (L ² /t ³)
263	θ	angle of the tube settler
264	λ	wavelength of incident light (L)
265	μ	dynamic viscosity of fluid [M/(L·t)]
266	ν	kinetic viscosity (L ² /t)
267	ν_{H_2O}	kinematic viscosity of water (L ² /t)
268	ρ_{clay}	density of primary clay particle (M/L ³)

269	ρ_{H_2O}	density of water (M/L ³)
270	Φ	shape factor for drags on flocs

271

CHAPTER 1: INTRODUCTION

272 The quality of water has a significant impact on both human health and socioeconomic
273 development. The criteria for access to sufficient water for domestic uses include, but are not
274 limited to the following: safety, reliability, sustainability, affordability and physical accessibility.
275 However, it is estimated by the United Nations (Millennium Development Goals Report, 2012)
276 that 783 million people, or 11% of the global population, do not have access to improved sources
277 of drinking water (such as house hold connections and public standpipes). In some rural areas,
278 even higher portions of the population lack access to improved drinking water and are exposed to
279 dangerous levels of biologically or chemically contaminated water due to inadequate water
280 treatment systems. Thus, technology to provide safe water for hundreds of millions of people at
281 low cost is in demand.

282 AguaClara is a multi-disciplinary program in the School of Civil and Environmental Engineering
283 at Cornell University that conducts laboratory research leading to the design of sustainable,
284 gravity-powered, electricity-free water treatment plants. The treatment processes include rapid
285 mix, flocculation, sedimentation, filtration and disinfection. AguaClara designs of water
286 treatment plants constructed in Honduras provide clean water that meets the guidelines of the
287 World Health Organization in a cost-effective way. Ten communities consisting of 40,000
288 people are served by AguaClara technologies and it is anticipated that more people will benefit
289 from this program in the near future (AguaClara, 2015).

290 The research in this thesis is a part of AguaClara program and it presents development of a non-
291 intrusive imaging process as a tool for measurement of flocs formed through flocculation and
292 clarified by sedimentation. Natural water sources contain inorganic and organic particles
293 including pathogens, which are harmful to human health. Flocculation and sedimentation are
294 important parts of drinking water treatment in that they can remove these particles. Flocculation
295 is a process where colloids aggregate and form flocs that are removed by gravity forces in the
296 sedimentation tank. However, many of the fundamental mechanisms that control flocculation are
297 not well understood. For example, experimental data from the AguaClara research team suggests
298 use of a mechanistic model where small particles do not readily attach to big flocs. There appears
299 to be something about the collisions between particles that are very different in size that makes
300 aggregation difficult. Observation of floc collisions may inform our understanding of factors
301 that inhibit aggregation.

302 The objectives of this research were to develop non-destructive imaging techniques that permit
303 floc characterization and to study the influence of coagulant dose on floc size distribution and
304 turbidity removal. The variances in particle size distributions under different operating
305 conditions can be of use in the understanding of aggregation mechanisms. Understanding how
306 floc size distribution influences the flocculation process and removal of particles by
307 sedimentation will contribute to the optimization of treatment plant design. The development of
308 the image analysis tool also lays a foundation for future studies of particle collisions and the
309 mechanisms that control aggregation.

310

311

312

CHAPTER 2: CHARACTERIZATION OF FLOCS

313

AND FLOC SIZE DISTRIBUTION¹

314

2.1 Abstract

315

A nonintrusive digital imaging process was developed to study particle size distributions created

316

through flocculation and sedimentation. This process was calibrated by measuring standardized

317

polystyrene particles of known size and was utilized to count and measure individual kaolin clay

318

particles as well as aggregates formed by coagulation with polyaluminum chloride and

319

flocculation. Identification of out-of focus flocs was automated with LabVIEW and used to

320

remove them from the database that was analyzed. The particle diameter of the test suspension of

321

kaolinite clay was measured to be $7.7 \pm 3.8 \mu\text{m}$ and a linear relationship was obtained between

322

turbidity and the concentration of clay particles determined by imaging. The analysis technique

323

was applied to characterize flocs and floc particle size distribution as a function of coagulant

324

dose. Removal of flocs by sedimentation was characterized by imaging and the negative

325

logarithm of the fraction of turbidity remaining after settling had a positive linear association

326

with the logarithm of aluminum dose. The maximum floc size observed in the settled water was

¹The content of this chapter will be submitted to *Environmental Engineering Science*, with co-authors M. L. Weber-Shirk and L. W. Lion.

327 less than 120 μm , which was in accordance with the value predicted by a terminal velocity model
328 for the capture velocity of the experimental tube settler of 0.21 mm/s.

329 **2.2 Introduction**

330 Flocculation facilitates aggregation of inorganic and organic particles in water sources, and is a
331 crucial pretreatment process prior to particle removal by sedimentation and filtration. The fluid
332 velocity gradient (G) is widely recognized as a key design parameter for laminar flow
333 flocculators. Many studies have shown a relation between floc sizes and G (Park et al., 1972;
334 Matsuo and Unno, 1981; Hopkins and Ducoste, 2003). Gregory (1981) and Camp and Stein
335 (1943) proposed two different ways to calculate G, in terms of a given flow rate and tube
336 diameter. For the conditions of this research, the average velocity gradient calculated by Camp
337 and Stein (70.6/s) is 6% higher than that by Gregory (see calculations in Appendix A.). Energy
338 dissipation rate (ε) is also used in the design of water treatment plants and, under conditions of
339 laminar flow, is related to \bar{G} , as follows (Coufort et al., 2008):

$$340 \quad \bar{G} = \sqrt{\frac{\varepsilon}{\nu}} \quad (1)$$

341 Where, ε is the average energy dissipation rate, and

342 ν is the kinematic viscosity of fluid.

343 During flocculation, particle sizes, structures and shapes can all affect aggregation behavior and
344 collision efficiency (Jiang and Logan, 1991). Yao et al. (2014) reported that concentration of
345 particles less than 5 μm is in a positive linear relationship with water turbidity in the range of 0-

346 40 Nephelometric Turbidity Units (NTU). Nan et al. (2009) suggested that flocs in different size
347 ranges contribute differently to the decrease in turbidity after sedimentation. Thus, the
348 measurement of particle size distribution during flocculation can be of use in understanding
349 particle removal subsequent to flocculation.

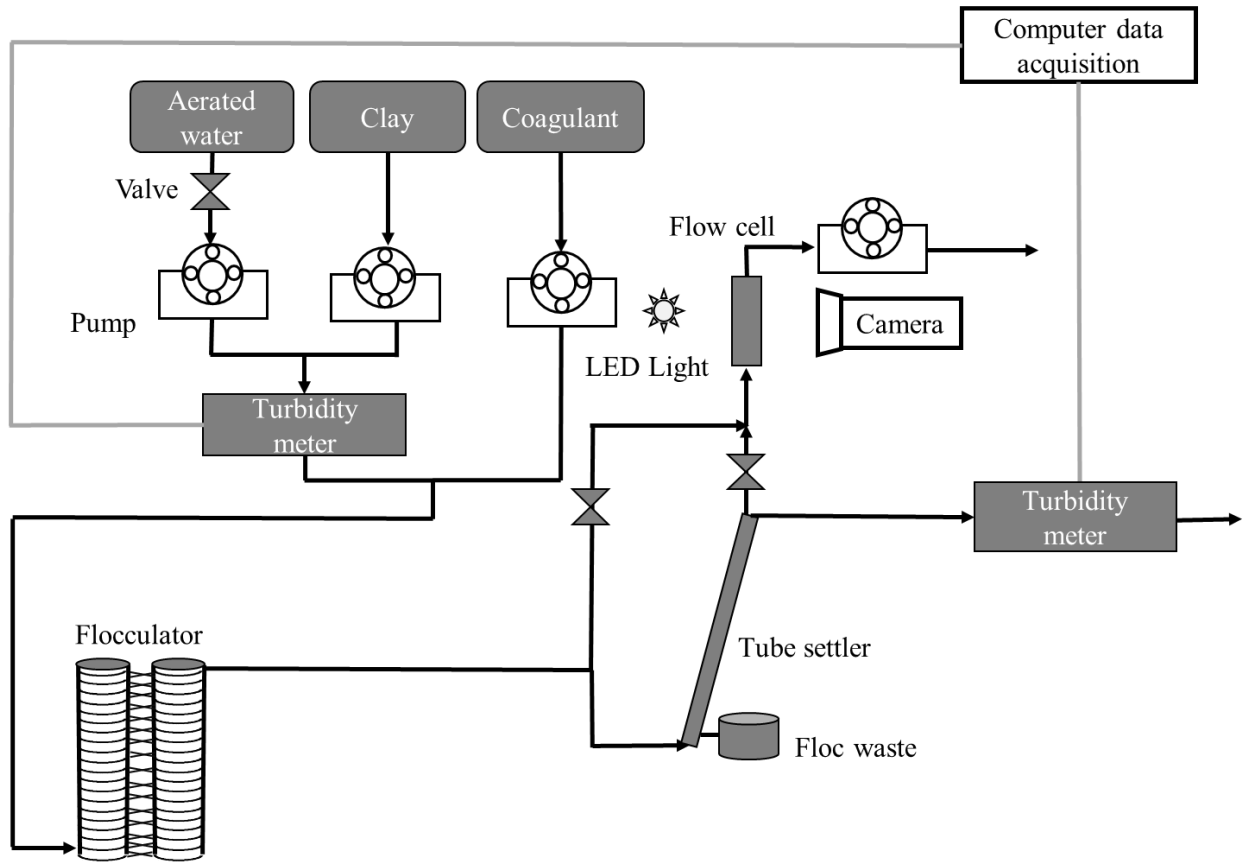
350 Particle size characterization can be accomplished using a Coulter counter (Zhang et al., 2007) or
351 by the electrical sensing zone method (Gibbs, 1982). However, both analyses require withdrawal
352 of samples from a suspension that may disrupt fragile flocs (Chakraborti et al., 2000). Some
353 researchers have adopted photographic techniques and image analysis as a non-invasive tool for
354 the continuous measurement of changes in floc sizes in jar tests. Bouyer et al. (2004) used a laser
355 beam as light source and VISILOG 5 for image analysis to obtain the instantaneous size
356 distribution of flocs. However, they found it difficult to exploit the data without analyzing the
357 contour of particles because there were too many possible intersections between the laser plane
358 and particle shapes, and particle data needed to be discarded if the contour of the particle was
359 shaded. PIV (particle image velocimetry) software for image acquisition and storage and NIH-
360 Image software for image analysis have been used by Chakraborti et al. (2000) to characterize
361 alum flocs. Keyvani and Strom (2013) developed a fully automated image processing script to
362 remove out-of focus particles to attain more precise size distributions with Image J and
363 MATLAB.

364 Based on Keyvani and Strom's study, an image analysis script was developed in this research
365 using National Instruments LabVIEW and Vision Builder Toolkit to explore particle size
366 distribution changes during flocculation and sedimentation. The LabVIEW software
367 incorporates image acquisition and analysis.

368 **2.3 Experimental Methods**

369 **2.3.1 Flocculator Setup**

370 Figure 1 shows a schematic of the laboratory apparatus. Aerated water was pumped from a
371 temperature-controlled reservoir and mixed with a concentrated kaolinite (R.T. Vanderbilt Co.,
372 Inc. Norwalk, CT.) clay stock to form synthetic raw water. Raw water turbidity was controlled
373 by adjusting the flow rate of clay stock (see equation 25 in the Appendix B.) and was
374 continuously measured using a MicroTOL 3 turbidity meter (Model number: 20055, HF
375 Scientific, Inc. FT. Myers, FL.). The turbidity meter was equipped with a flow cell so that there
376 was no need to withdraw samples from the raw water. Polyaluminum chloride (PACl) coagulant
377 doses (Holland Company. Adams, MA.) ranging from (0.53 to 2.65 mg/L as Al) were mixed into
378 the raw water. Flocculation was accomplished by laminar flow through a coiled 9.52 mm (inner
379 diameter) tube. The average energy dissipation rate of the flocculator was 5 mW/kg and the
380 hydraulic residence time was 300 s. Sedimentation occurred in a tube settler with a capture
381 velocity (also referred to as a critical velocity) of 0.21 mm/s. Approximately 8% of the
382 experimental flow could be directed to a flow cell. Two valves were utilized to control the type
383 of water entering the flow cell allowing imaging of either flocculated water or settled water.
384 Effluent turbidity was continuously measured using MicroTOL 2 turbidity meter (Model number:
385 20053, HF Scientific, Inc. FT. Myers, FL.). Process Controller software created using LabVIEW
386 by Weber-Shirk (2008) was utilized for acquisition of turbidity data.



387

388 **Figure 1. Schematic of the experimental apparatus.**

389 In laminar flow, there is no turbulence to resuspend particles that may settle in the flocculator.

390 As a result, the experimental flocculator tubing was coiled in a figure eight configuration to

391 create a secondary flow circulation to prevent floc sedimentation (Tse et al., 2011).

392 The average velocity gradient (\overline{G}_c) in the coiled figure eight flocculator that accounts for the

393 secondary flow was calculated as described by Tse et al. (2011):

394
$$\overline{G}_c = \overline{G} \sqrt{1 + 0.033 \left[\log \left(\frac{4Q_{plant}}{\pi Dv} \sqrt{\frac{D}{R_c}} \right) \right]^4}$$
 (2)

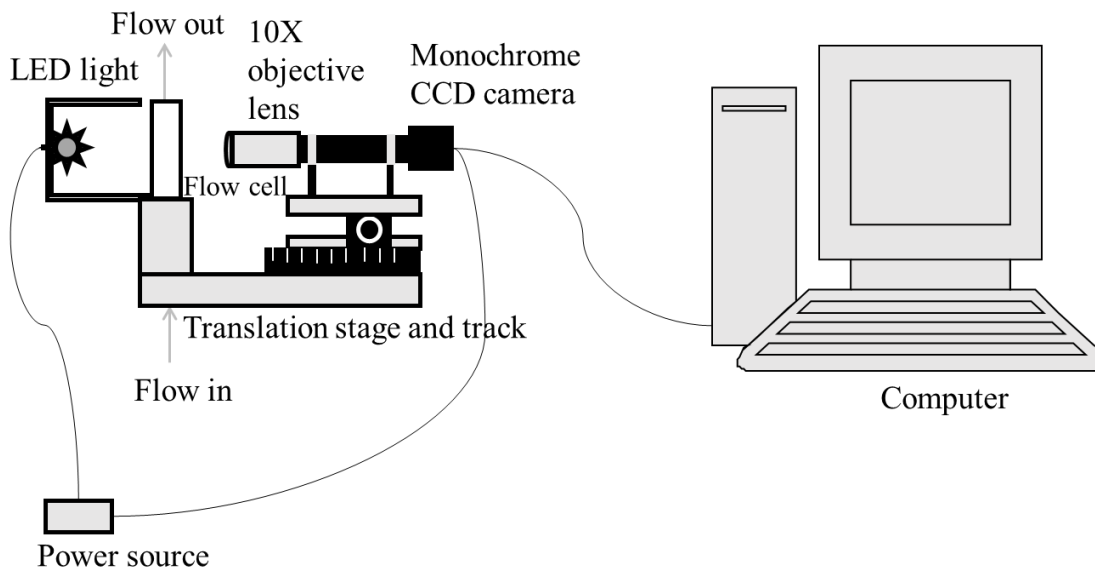
395 Where Q_{plant} is the experimental flow rate,

396 D is the inner diameter of the flocculator tube, and

397 R_c is the diameter of curvature of the flocculator coils.

398 2.3.2 Imaging system

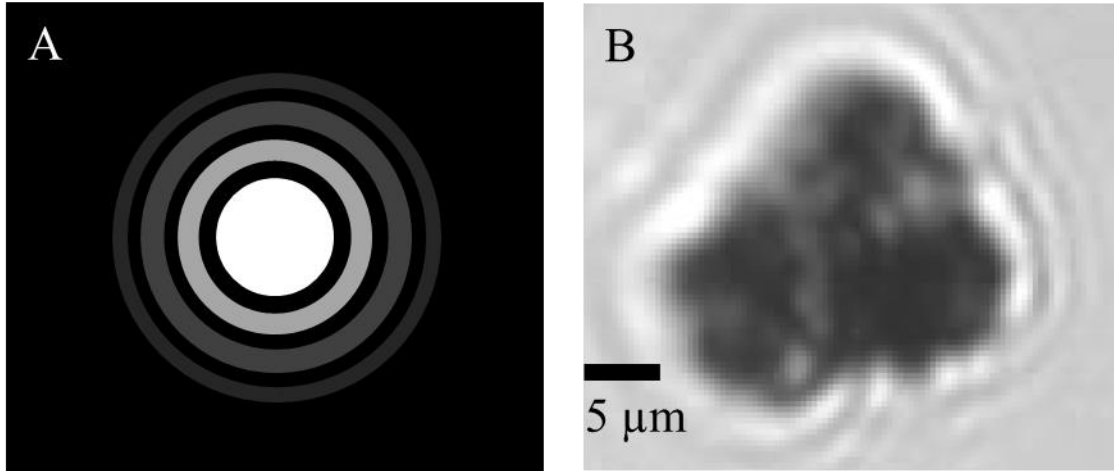
399 The camera system (see Figure 2) consisted of an LED light source and a Flea3 FL3-GE-13S2M
400 monochrome GigE camera (Point Grey Research, Inc. Richmond, BC, Canada) controlled by the
401 LabVIEW program. The camera was a 1288×964 pixel progressive scan, monochrome 1/3” CCD
402 fitted with an M Plan Apo 10× infinity-corrected objective lens with a numerical aperture of 0.28
403 (Mitutoyo Corporation, Japan). The camera can capture continuous images at up to 31 frames per
404 second or single images by external trigger or via software control.



405

406 **Figure 2. Imaging system consisting of LED light, CCD camera attached to a computer and**
407 **the suspended sample in a flow cell.**

408 Based on the camera sensor format and 10× magnification of the objective lens, the field of view
409 for the imaging system was 480 μm×360 μm. Each pixel sampled an area in the field of view of
410 0.375 μm by 0.375 μm. The depth of field of the objective lens was calculated over a range of
411 influent turbidities and the average value was 500 ± 90 μm (See equation (11) in part 2.6.1). The
412 constraints for maximum floc size measurements are the field of view and the depth of field of
413 the lens. For flocs smaller than this depth of field, it is likely that the entire floc will be in focus.
414 Since the size of one pixel is close to the wavelength of visible light (approximately 400-700 nm)
415 (Pal and Pal, 2001), the diffraction of light can result in airy disks around particles in images and
416 errors in particle size measurements. An airy disk is a bright central core surrounded by
417 diffraction rings. More than 80% of light energy concentrates in the central ring of the airy disk
418 (Greivenkamp, 2004), as the intensity distribution in Figure 3(A) shows.



419

420 **Figure 3. Airy disks. (A) Airy pattern and intensity distribution. (B) Airy patterns around a**
421 **particle.**

422 A consequence of the formation of airy disks is that a point in an object will not be imaged as a
423 spot with sharply defined edges. Instead, it is imaged by the objective lens as a spot surrounded

424 by diffraction rings, which can affect the accuracy in measuring particle diameters. Figure 3(B)
425 illustrates one example showing the airy patterns around a particle. It is obvious that the edges of
426 the floc are not sharply contrasted.

427 The radius of the central ring of the airy disk can be calculated by (“Wavelength effects on
428 performance”, 2015),

$$429 \quad r_{airy\ disk} = \frac{0.61\lambda}{NA} \quad (3)$$

430 Where λ is the wavelength of the incident light,

431 NA is numerical aperture, and was approximately 0.28 for the objective lens used in this
432 research.

433 The estimated radius of airy disk caused by yellow light ($\lambda \approx 590nm$) is around $1.29\ \mu m$. Since
434 each point around the particle has airy pattern, particles less than $1.29 \times 2 \approx 2.6\ \mu m$ in diameter
435 (particle area of approximately 39 pixels) cannot be clearly identified. The apparatus could thus
436 measure particle sizes ranging from $2.6\ \mu m$ (set by the airy disk) to more than $300\ \mu m$ (set by the
437 field of view). Standardized particles of known size were utilized to determine the error in
438 particle size measurement caused by light diffraction.

439 The camera was connected to the computer via Gigabit Ethernet, which allowed an acceptable
440 transfer speed of 100 MB/s (equivalent to 2226 images of JPEG format per second). The camera
441 was mounted on a horizontal translation stage fixed to an aluminum platform. An LED light
442 provided bright field illumination of flocs in the flow cell (Keyvani and Strom, 2013).

443 The flow cell was constructed from a glass cuvette with a cross sectional area of 1 cm × 1 cm.
444 The inlet and outlet of the flow cell had a diameter of 7.1 mm. The flow rate inside the flow cell
445 was constrained by the minimum shutter speed of the digital camera. It was assumed that blurry
446 images could occur when a pixel moved 1/4 of its length. Therefore, the maximum flow rate
447 inside the flow cell was calculated by equation (4).

$$448 \quad Q_{flowcell} = 0.375 \mu m \times \frac{1}{4} \times \frac{A_{flowcell}}{t} \quad (4)$$

449 Where, $A_{flowcell}$ is the cross sectional area of the flow cell and t is the time the shutter is open
450 (33 μs).

451 The flow rate through the sample cell was set to 0.28 mL/s based on equation (4). The average
452 velocity gradient in the inlet port of the flow cell was 5.4/s making the average velocity gradient
453 entering the flow cell less than 7.6% of the average velocity gradient in the flocculator. The
454 average velocity of the water flowing through the flow cell was 2.84 mm/s. This velocity was
455 also much higher than the sedimentation velocity of the largest flocs measured.

456 During initial testing of the imaging system the optimal shutter speed for image contrast was
457 determined to be 330 μs or 10 times longer than the minimum shutter speed. The particle travel
458 distance during this time is 1 μm and there was no evidence of significant image blurring. The 1
459 μm travel distance during the time when the shutter is open is small compared to the minimum
460 particle size of 2.6 μm.

461 **2.4 Image analysis**

462 The image analysis script accomplished four functions: (1) reduction of image noise, (2)
463 identification of particles from background, (3) removal of particles that were out of focus or that
464 had portions beyond the image border, (4) calculation and recording of particle sizes. The image
465 processing functions prepackaged in LabVIEW are capable of identifying and measuring
466 particles. These functions include filters, threshold, basic or advanced morphology and particle
467 analysis (“Image analysis and processing,” 2008).

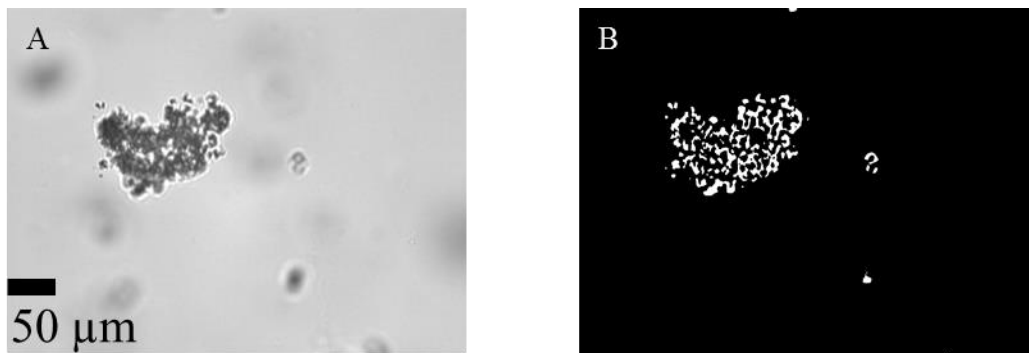
468 **2.4.1 Identification of particles**

469 A filter was first applied to each image to reduce small changes in pixel values caused by
470 variability in the charge-coupled device of the camera. The Gaussian filtering function of the
471 LabVIEW vision application was found to work best at reducing noise by attenuating the
472 variations of grey scale intensity in a pixel’s neighborhood. The Gaussian filter effectively
473 smoothed the fuzzy edge of the particles in the image so that one could better extract useful
474 information from a particular image.

475 Filtering was followed by the operation of thresholding, which distinguished particles from the
476 background and produced a binary image with 0 representing the background and 1 representing
477 particles. In general, there are two thresholding methods: global thresholding and local
478 thresholding. Global thresholding identifies particles based on a single grayscale value. In local
479 thresholding, each pixel is categorized based on the intensity of pixels in its neighborhood
480 (“Thresholding,” 2013). Global thresholding usually requires a specified threshold range for each

481 set of tests, while local thresholding can identify particles automatically. Thus, background
482 correction (“Thresholding”, 2013) within local thresholding function was utilized in the image
483 analysis procedure in this research in that this technique is well suited for conditions where
484 images exhibit nonuniform light intensities caused by other out of focus particles in the
485 background.

486 Figure 4 shows the application of local thresholding (background correction). This local
487 thresholding method appears to function well in particle recognition.

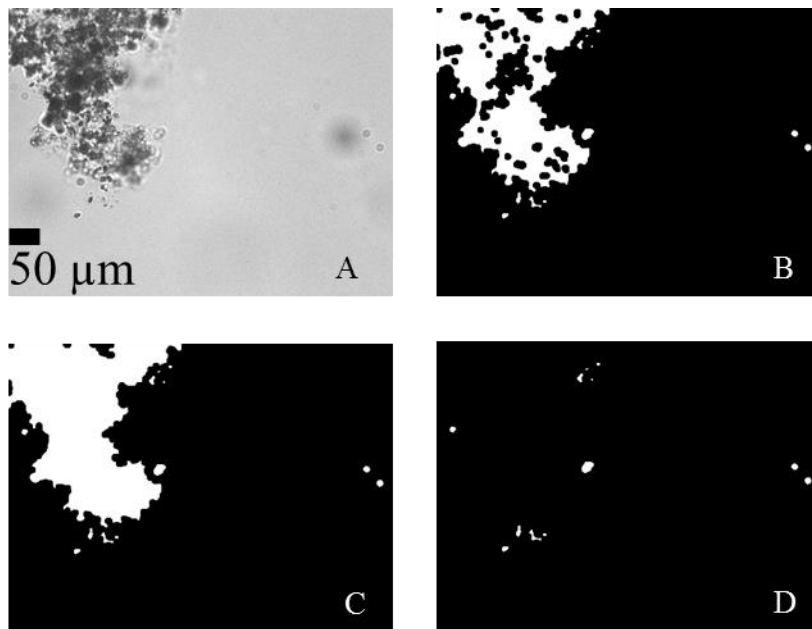


488
489 **Figure 4. Application of local thresholding. (A) The original image with flocs. (B) Local**
490 **thresholding applied to image A.**

491 When local thresholding is applied to an image, holes and gaps inside a floc can arise due to the
492 complicated structure of the aggregates. The holes and gaps must be filled to calculate the
493 particle area. Thus, some morphological transformations were utilized to prepare particle images
494 for quantitative analysis. These transformations included closing the object perimeter, filling
495 holes, and removing particles touching the border as well as small particles less than 39 pixels
496 (equivalent spherical diameter of 2.6 μm). Particles less than 39 pixels were not considered

497 because they were too small to obtain an accurate measurement of their shape and area as a result
498 of airy disc patterns.

499 The closing objects function was able to fill small holes and smooth the boundaries of the floc.
500 These changes only slightly alter the shape or the area of the object. The filling holes function
501 filled any remaining holes inside the particle boundary. Figure 5 shows an example of the
502 morphology transformation functions.



503

504 **Figure 5. Example of morphological transformation. (A) Original grey scale image, (B)**
505 **image after background correction and closing objects, (C) image after filling holes, (D)**
506 **image after removing small particles or particles that touched the border of the image.**

507 The next step in image analysis was to measure the area and the coordinates of the bounding
508 rectangle of each floc in pixels. The spherical–equivalent diameter in pixels can be calculated as,

509
$$d_{pixel} = \sqrt{\frac{4A_{pixel}}{\pi}} \quad (5)$$

510 Where A_{pixel} is the projected area of the particle, in pixels. As mentioned above, particle sizes
511 were also calibrated in this step to account for the influence of airy disks.

512 The Region of Interest (ROI) for each floc was defined by the coordinates of the bounding
513 rectangle. The floc ROI of the original image was used to assess if the floc was in focus.

514 **2.4.2 Removing out-of focus particles**

515 As noted above, local thresholding could identify almost all particles within an image regardless
516 of their degrees of focus, except for some extremely blurry flocs, such as the ones in Figure 4(A).
517 Hence, the next part of the image analysis script acted to remove out-of focus flocs.

518 Whether an object in an image appears blurry or not is determined by its focus quality
519 characterized by the sharp differences between background and object edges (Klinger, 2003).
520 Keyvani and Strom (2013) introduced a concept of “clarity value” index to determine the focus
521 quality of each floc and thus distinguish in-focus particles from the blurry ones. In their work,
522 each image was treated with a convolution of a first Gaussian kernel in both horizontal and
523 vertical directions. The maximum value of the filtered image associated with each floc could be
524 used to define how close the floc was to the focal plane.

525 Flocs that are in focus have sharp gradients between the background and the floc. Flocs that are
526 out of focus have weaker gradients at their boundaries. The image gradient intensity at the floc
527 boundaries was used to eliminate flocs that were not in focus. The sobel filter computes an
528 approximation of the image intensity gradient. High sobel filter values indicated the floc was in
529 focus. The maximum image intensity gradient was computed for each floc. In order to eliminate

530 the effect of LED light intensity and shutter speed (which will have influence on the light
 531 intensity), the maximum image intensity gradient was divided by the mean pixel value of the
 532 whole image. The result was then multiplied by a length scale ($3 \times 0.375 \mu\text{m}$) related to kernel size
 533 (a kernel is a 3×3 matrix for a sobel filter) to give in a dimensionless parameter used to
 534 discriminate between in focus and out of focus floccs.

$$535 \quad \alpha = \frac{\min[I(ROI_i)]}{\text{mean}[I(ROI_i)]} \quad (6)$$

$$536 \quad \beta = \frac{\max[I_f(ROI_i)] \times l}{\text{mean}[I(ROI_i)]} \quad (7)$$

537 Where, α is the normalized minimum pixel value,

538 I is the matrix of the original image pixel values,

539 ROI_i is the bounding rectangle of floc i ,

540 β is the dimensionless maximum floc image intensity gradient,

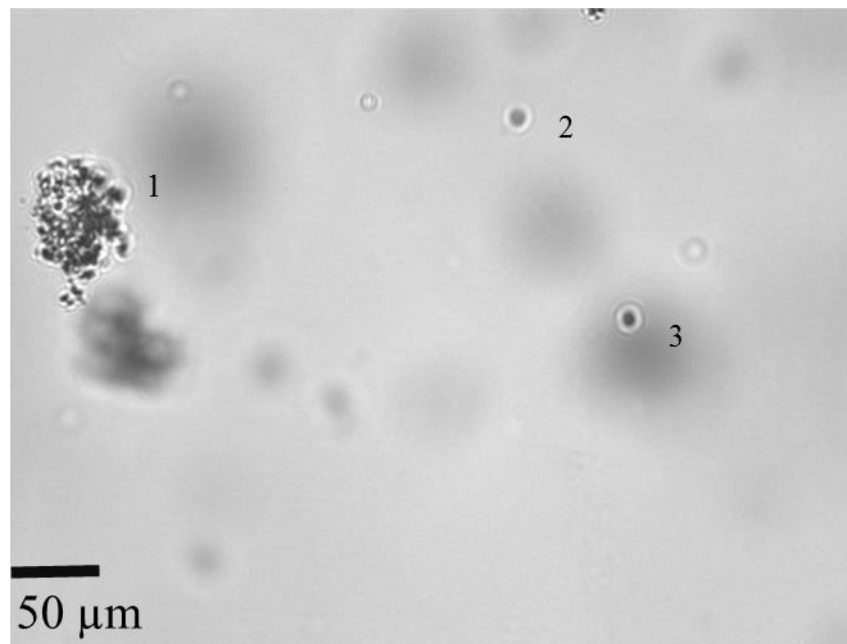
541 I_f is the sobel filter of the image matrix,

542 l is the length scale of the sobel filter kernel, which is $1.1 \mu\text{m}$.

543 Darker floccs (which have smaller pixel values) were closer to the focal plane. Thus, the
 544 minimum pixel value (α) of I (the original image matrix) associated with each floc was also
 545 measured to assist in the determination of focus quality. Some transparent particles of unknown
 546 origin were observed in the clay mixture with a β greater than 0.16. These unknown particles
 547 were discarded by setting a minimum pixel value of I . The minimum pixel value of the original
 548 image was normalized to be dimensionless as described above.

549 Threshold values for both α and β were used to distinguish in-focus particles from those which
550 were not in focus and were determined by examining computed values from a great number of
551 images. After comparison, the image intensity gradient threshold value (β_t) was set to be 0.16
552 and the threshold value of the normalized minimum pixel value (α_t) to be 0.56. Therefore,
553 particles with β above 0.16 and α below 0.56 were considered as in focus floccs and the remaining
554 floccs were removed from the database. The calculated spherical-equivalent diameters of those in-
555 focus floccs were then written to a cvs file for each image.

556 Figure 6 and Figure 7 are two examples showing different α and β values and the focus quality
557 within an image.



558

559 **Figure 6. Sample image of identified and measured floccs.**

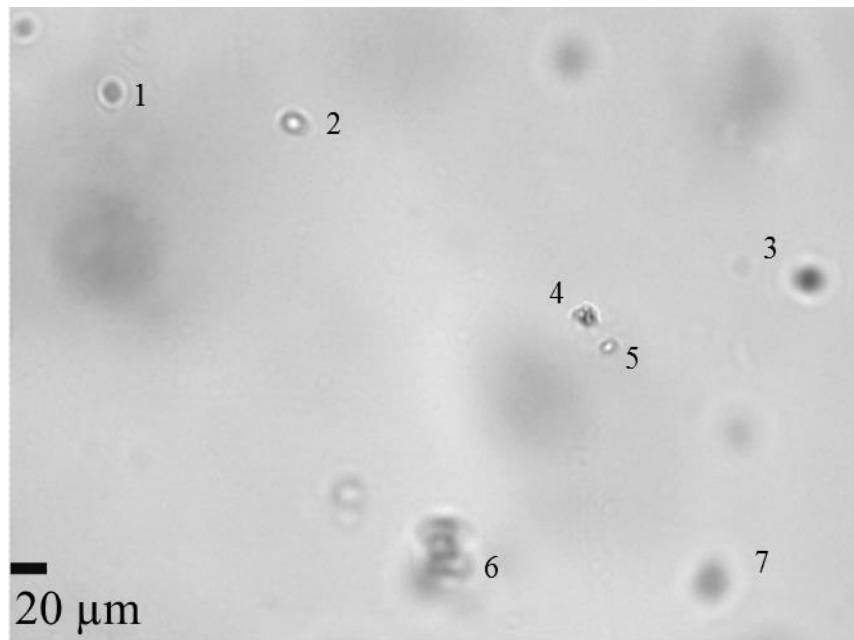
560 For Figure 6, three floccs are identified after thresholding (actually four particles were identified,
561 however one touching the top border was removed). Floc 1 has the best focus quality; floccs 2 and

3 may possibly be in-focus. As is shown in Table 1, a value of $\beta_t = 0.16$ and a value of $\alpha_t = 0.56$ worked well as a particle filter, removing the out-of focus floccs and retaining the in-focus ones.

Table 1. Identified floccs in Figure 6 with their associated α and β values. Bold values meet the constraints.

Floc number	α	β	Acceptable	Spherical diameter (μm)
1	0.26	0.69	Yes	56.4
2	0.65	0.15	No	---
3	0.37	0.20	Yes	6.9

Figure 7 is another example showing how the algorithm performed. There are seven particles detected in the image.



568

Figure 7. Sample image of identified and measured floccs.

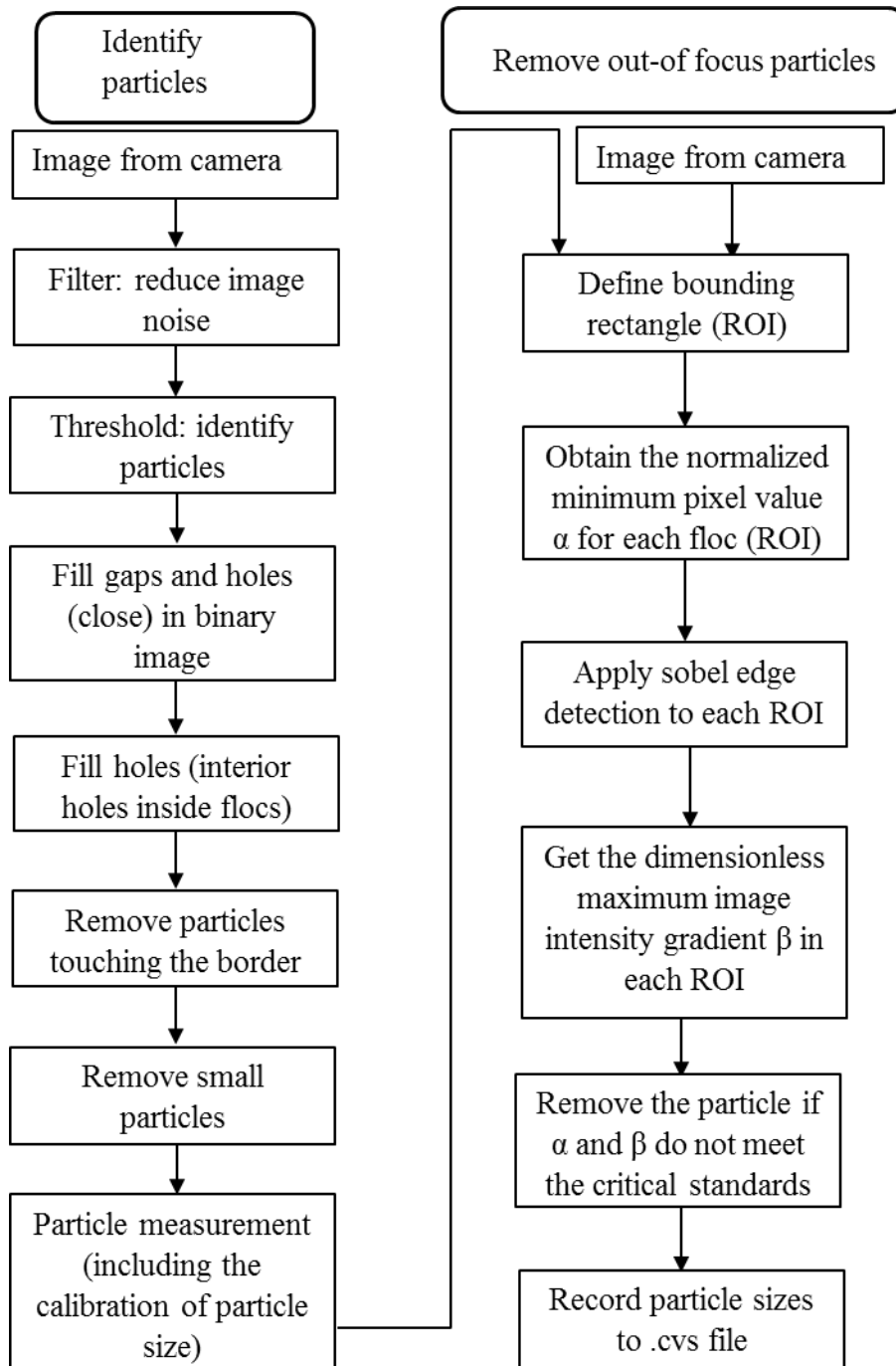
569

570 However, by visual observation, one could easily conclude that there is only one in-focus flocc
571 (floc 4), which agrees with the result in Table 2.

572 **Table 2. Identified floccs in Figure 7 with their associated α and β values. Bold values meet**
573 **the constraints.**

Floc number	α	β	Acceptable	Spherical diameter (μm)
1	0.69	0.13	No	---
2	0.69	0.19	No	---
3	0.48	0.09	No	---
4	0.38	0.41	Yes	11.8
5	0.74	0.27	No	---
6	0.66	0.08	No	---
7	0.76	0.04	No	---

574 Figure 8 summarizes the order of operations performed on each image to obtain the geometric
575 characteristics of particles.



576

577

Figure 8. Flowchart of image analysis procedure.

578

579 **2.5 Terminal velocity**

580 Terminal velocity is the velocity of a floc when the forces of gravity and drag plus buoyancy are
581 equal. Flocs are very likely to be captured by settling if their terminal velocity is higher than the
582 capture velocity of the settling tube.

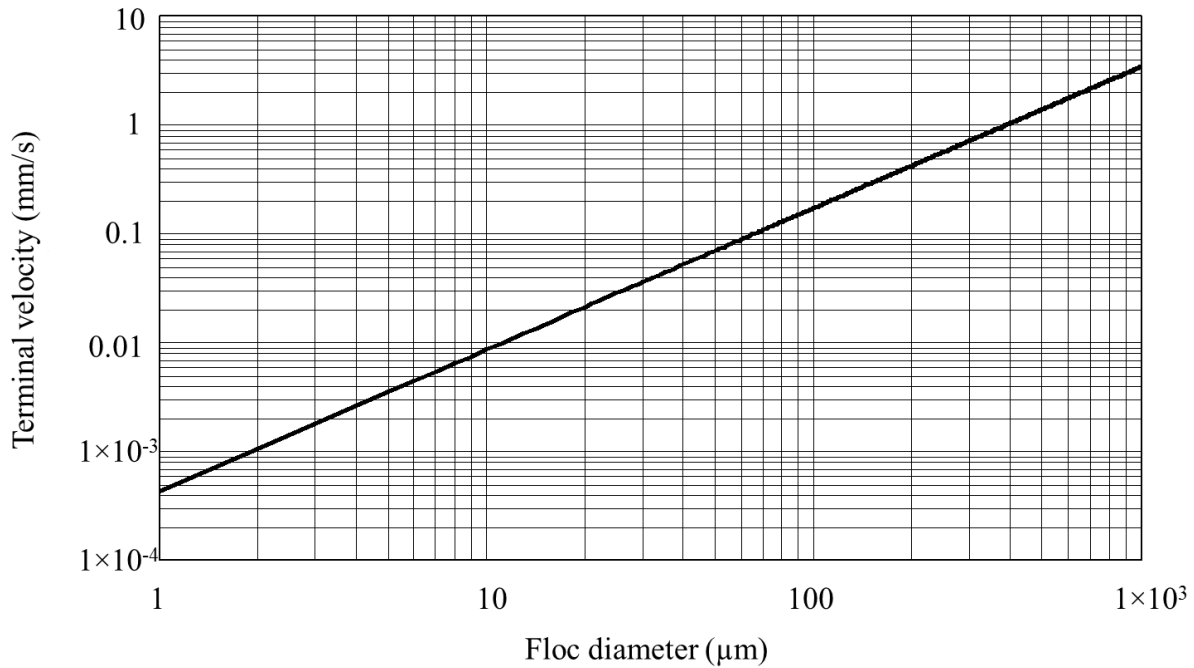
583 The terminal settling velocity for flocs was defined by Adachi and Tanaka (1997) as:

$$584 \quad v_t = \frac{g d_{clay}^2}{18 \Phi \nu_{H_2O}} \frac{\rho_{clay} - \rho_{H_2O}}{\rho_{H_2O}} \left(\frac{d}{d_{clay}} \right)^{D_{fractal} - 1} \quad (8)$$

585 Where Φ is the shape factor for drag on flocs, d is the diameter of floc, ν_{H_2O} is the kinematic
586 viscosity of water, ρ_{clay} is the density of primary clay particles, ρ_{H_2O} is the density of water,
587 d_{clay} is the diameter of the primary particles, d is the floc diameter, and $D_{fractal}$ is the 3-D
588 fractal dimension of flocs. The shape factor accounts for the adjustment of the coefficient of drag
589 for non-spherical geometry and has a fractional value of 45/24 (Adelman et al., 2013).

590 Li and Ganczarczyk (1989) calculated the fractal dimensions of the alum aggregates based on the
591 reported data of settling tests and size-density relations. The fractal dimension from Boadway's
592 (1978) data is calculated to be around 2.3 and the one from Tambo and Watanabe (1979) is
593 between 1.59-1.97.

594 Figure 9 shows settling velocities predicted by equation (8) using a fractal dimension of 2.3.



595

596

Figure 9. Terminal velocity versus floc diameter.

597 In the experimental tube settler the removal efficiency of slow settling flocs of a specific size can
 598 be quantified by pC^* , which is defined by the following equation,

599
$$pC^* = -\log_{10} \left(\frac{C_{effluent}}{C_{influent}} \right) \quad (9)$$

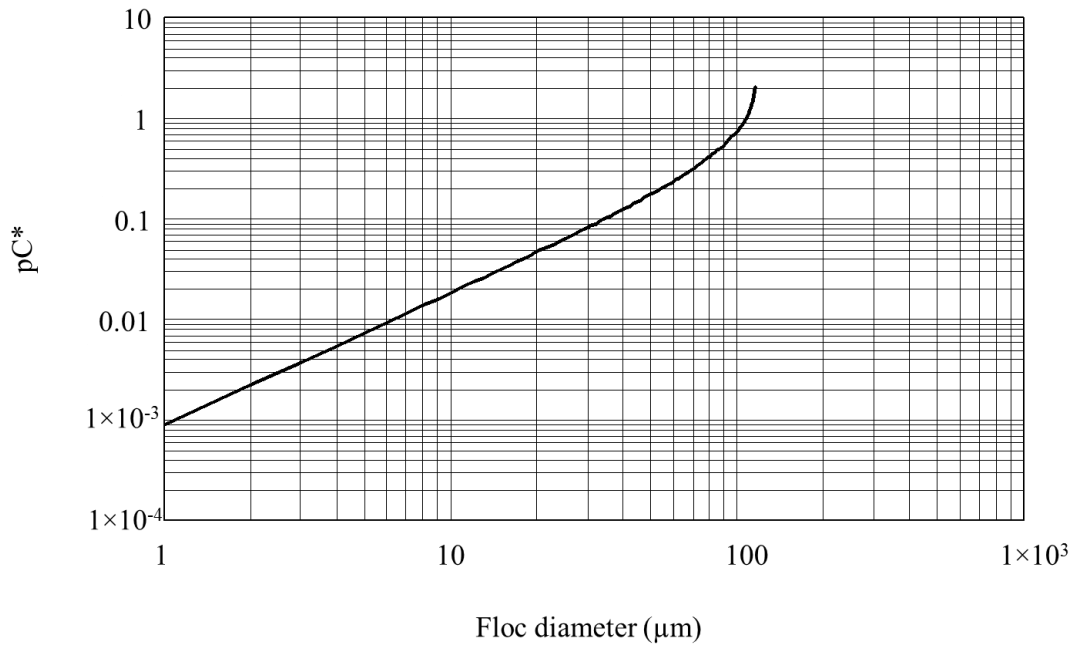
600 Where,
$$\frac{C_{effluent}}{C_{influent}} = 1 - \frac{v_t}{v_{capture}} \quad (10)$$

601 $C_{effluent}$ is the fraction of the effluent turbidity caused by the floc size class,

602 $C_{influent}$ is the fraction of the influent turbidity caused by the floc size class,

603 $v_{capture}$ is the capture velocity of tube settler.

604 Use of the ratio of terminal settling velocity and capture velocity to quantify removal of a floc
605 size class assumes that flocculation of particles does not occur in the tube settler. Figure 10
606 shows the expected pC^* as a function of floc size, based on the predicted tube settler
607 performance for the ratio of terminal velocity to capture velocity.



608

609

Figure 10. pC^* versus floc size.

610 Floccs larger than 120 μm have a terminal velocity greater than capture velocity of tube settler of

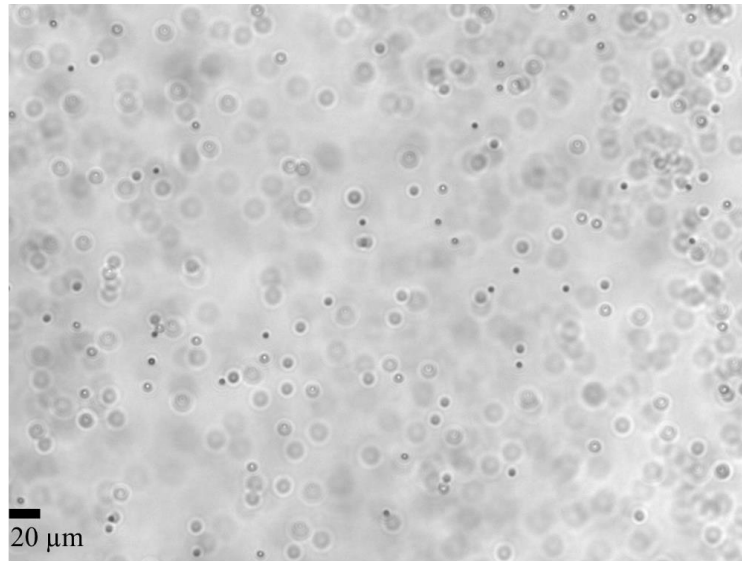
611 0.21 mm/s, which means the removal efficiency of those floccs is expected to be 100%.

612 **2.6 Results**

613 **2.6.1 Validation of image analysis method**

614 The clay particle used for the test was kaolinite. Kaolinite particles have a reported diameter
615 ranging from 0.2 μm to 12 μm (Aroke et al., 2013). The mean volume diameter of a 100 mg/L
616 kaolinite suspension (the turbidity was 68 NTU) was measured by a Mastersizer 2000 as 7.28
617 μm (Wei et al., 2015). Since the size of one pixel is close to the wavelength of visible light
618 (approximately 400-700 nm) (Pal and Pal, 2001), the diffraction of light can result in airy disks
619 around particles in images and errors in particle size measurements.

620 Therefore, sizes of standardized particles were tested to determine the error caused by light
621 diffraction in the camera setup. More than 300 images of the suspensions of dark blue
622 polystyrene particles with nominal size of 3.0 μm (Sigma-Aldrich, Switzerland) were captured.
623 Figure 11 is an example image of the standardized micro particles taken by the camera setup.



624

625 **Figure 11. Image of standardized 3 μm polystyrene particles taken by the camera setup.**

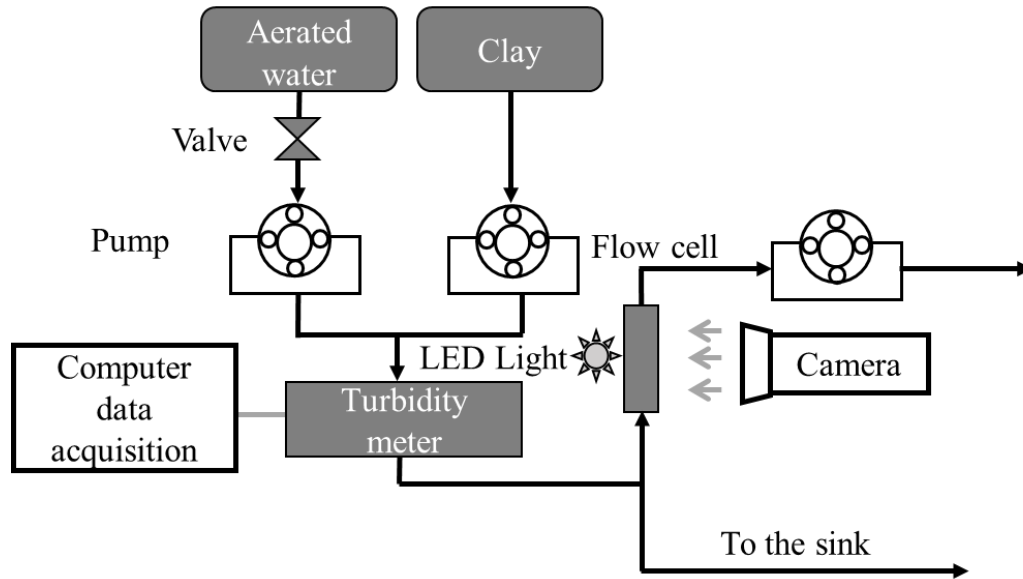
626 The images were then processed using the image analysis tool. The manufacturer determined the
 627 diameter of the standardized micro particles using a Coulter multisizer II. As is shown in Table
 628 3, the average particle size measured by the image system was greater than the values obtained
 629 by the manufacture by 2.6 μm, which was consistent with the estimated diameter of the airy disk.

630 **Table 3. Mean and standard deviation for 3.0 μm standardized particles**

3.0 μm particles	Coulter multisizer (μm)	Image analysis (μm)
Mean	2.83	5.45
Standard deviation	0.07	1.09

631 The image analysis method was then used to measure the diameter of clay particles at different
 632 turbidities in the absence of coagulant, with the apparatus configured as shown in Figure 12.

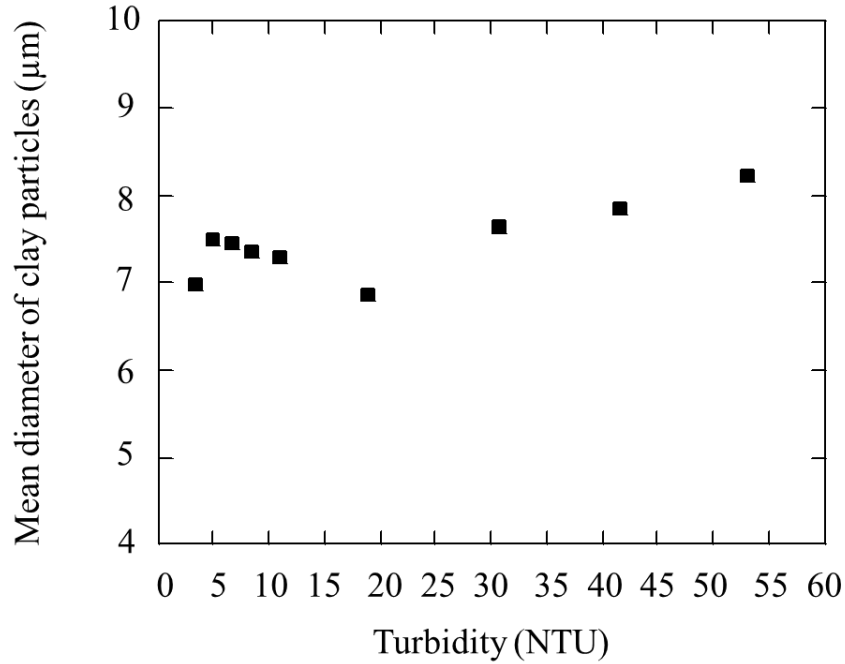
633 Based on the calibration, a correction of 2.6 μm was subtracted from the mean diameter
 634 measured by the image analysis software. Calibration of particles of larger sizes can be applied
 635 in future study to verify the accuracy of the correction value of 2.6 μm.



636

637 **Figure 12. Schematic of experimental set up for image analysis method verification.**

638 The average measured diameter of the test clay particles was $7.7 \pm 3.8 \mu\text{m}$ after correction for the
 639 airy disk, which was within the reported size range for kaolinite and was quite close to the mean
 640 diameter of $7.28 \mu\text{m}$ measured by Wei et al. (2015). Figure 13 illustrates the average measured
 641 clay diameters at different turbidities.



642

643

Figure 13. Average diameter of clay particles at different turbidities.

644

The depth of field of the lens is not specified by the manufacturer but it can be estimated. The

645

depth of field is expected to be a function of the β_{Min} value used to identify which flocs are

646

sufficiently in focus for further analysis.

647

The depth of field, H_{image} , could be derived from the following equation,

648

$$H_{image} = \frac{V_{clay} \cdot \rho_{clay}}{1.73 \frac{mg}{L \cdot NTU} \cdot Turbidity \cdot W_{image} \cdot L_{image}} \quad (11)$$

649

where W_{image} is the width of the image,

650

L_{image} is the height of the image,

651

V_{clay} is clay volume measured in one image based on the assumption that the clay

652 particles were spheres,

653 ρ_{clay} is clay density and has a value of 2.5 g/cm^3 ,

654 $1.73 \frac{\text{mg}}{\text{L}\cdot\text{NTU}}$ was measured in the Cornell Environmental Engineering laboratory by Casey

655 Garland (personal communication, June 13, 2015). This is similar to the value of $1.5 \frac{\text{mg}}{\text{L}\cdot\text{NTU}}$

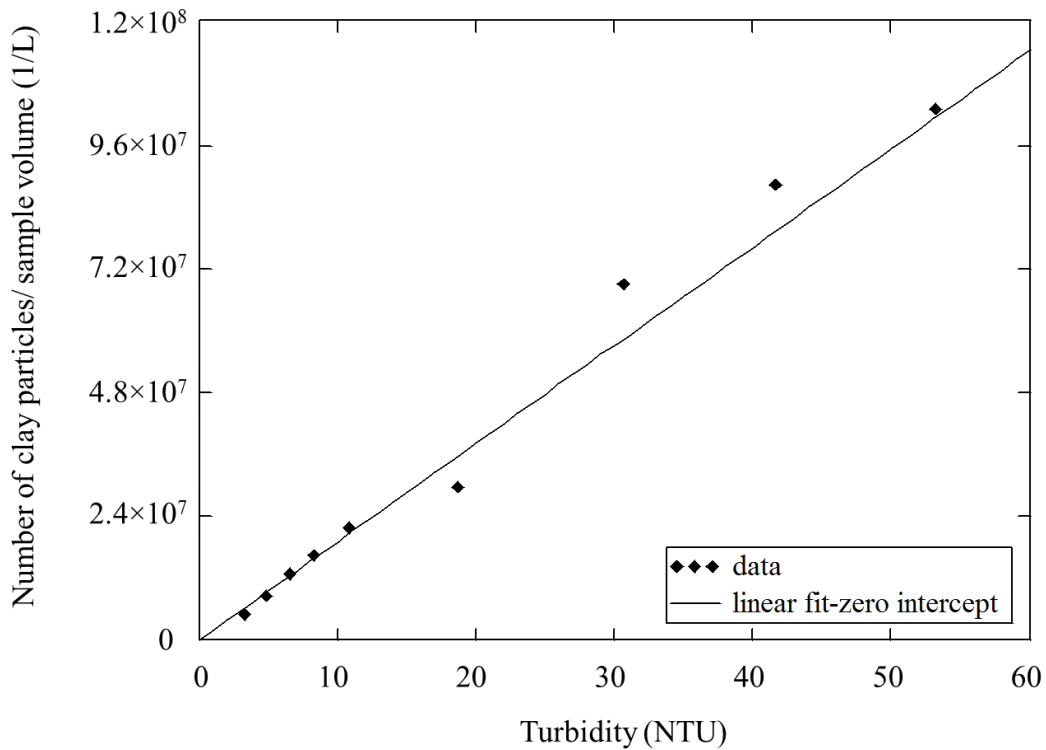
656 obtained by Wei et al. (2015).

657 The depth of field was calculated to be $500 \pm 90 \mu\text{m}$ for a range of influent turbidities. For flocs

658 smaller than this depth of field, it is likely that the entire floc will be in focus.

659 Figure 14 shows that there was a linear relationship between turbidity and the number

660 concentration of clay particles based on the depth of field calculated previously.



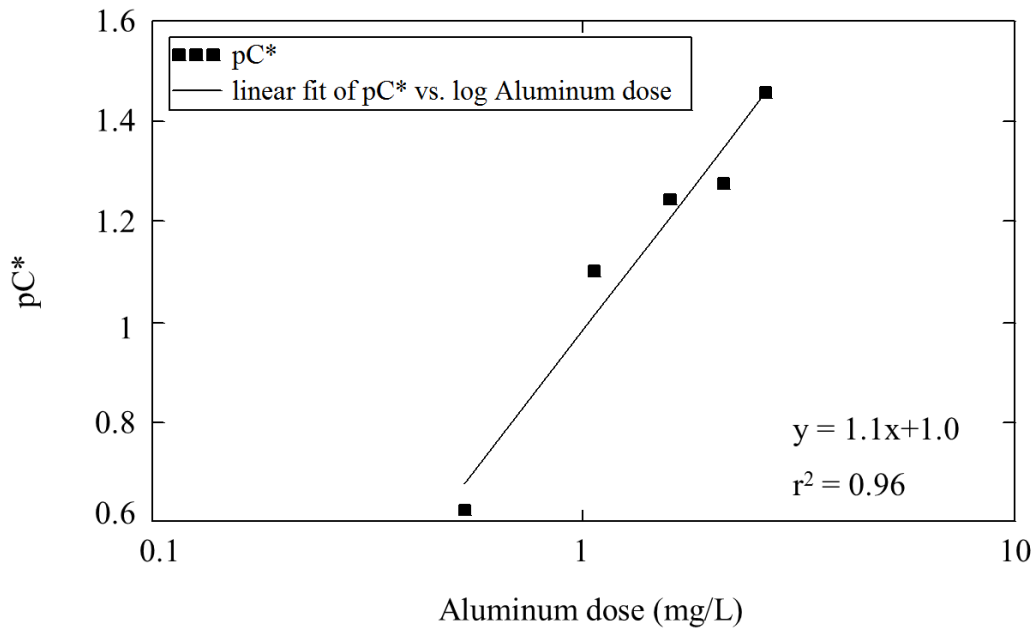
661

662 **Figure 14. Number of clay particles per sample volume versus turbidity.**

663 A linear fit with a zero intercept was obtained by calculating the average slope between each data
664 point and the origin. The slope of the linear fit was $1.9E6 \pm 2.2E5 \frac{1}{L \cdot NTU}$. Thus there were 1.9
665 million clay particles per $L \cdot NTU$. A $L \cdot NTU$ is equivalent to 1.73 mg of clay and given the
666 density of clay is equivalent to a clay volume of 0.68 μL . Thus the average volume of the clay
667 particles was $360 \mu\text{m}^3$ which yields an equivalent diameter of 8.8 μm . This is the volume
668 weighted average diameter of the clay particles and thus gives a slightly larger diameter than the
669 count weighted average diameter of $7.7 \pm 3.8 \mu\text{m}$.

670 **2.6.2 Effect of coagulant dose**

671 Image analysis was performed on settled water along with measurement of effluent turbidity.
672 Figure 15 shows pC^* values over a range of PACl doses. A pC^* value of 1 indicates 90%
673 removal efficiency a pC^* of 2 indicates 99%, and so on. The PACl doses applied to a 50 NTU
674 raw water were 0.53 mg/L, 1.06 mg/L, 1.59 mg/L, 2.11 mg/L and 2.65 mg/L as aluminum. As is
675 shown in Figure 15, pC^* increased when PACl dose increased and there was a linear relation
676 between pC^* and the logarithm of PACl dose.



677

678

Figure 15. pC* versus PACL dose (mg/L as Al).

679

The result in Figure 15 agree with the flocculation model created by Swetland et al. (2014).

680

These investigators observed a linear relationship between pC* and the logarithm of colloid

681

surface coverage by coagulant (which is proportional to coagulant dose at low doses). The slope

682

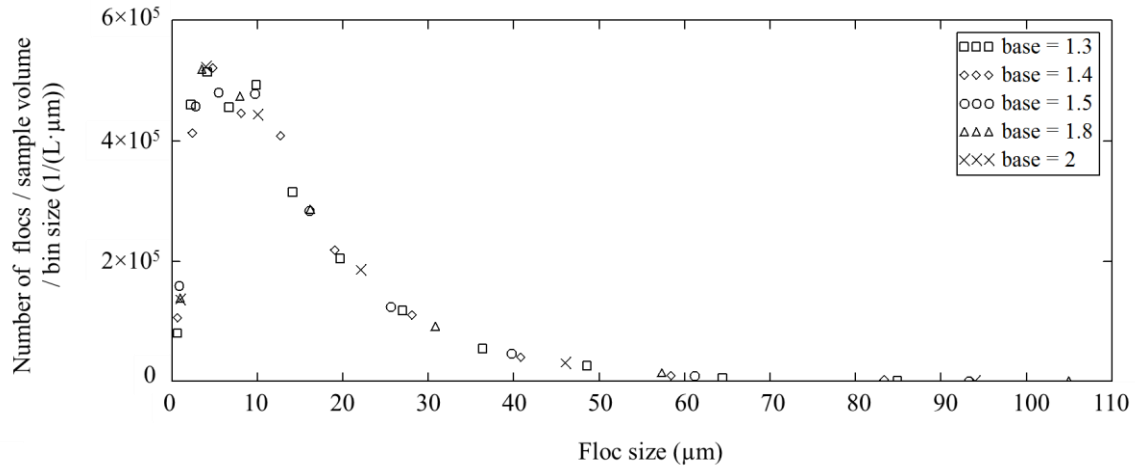
in Figure 15 was 1.1 and is close to the slope of 1 for the model indicated by Swetland et al.

683

(2014).

684

Figure 16 illustrates the distribution of floc number concentration allocated to different bin sizes.



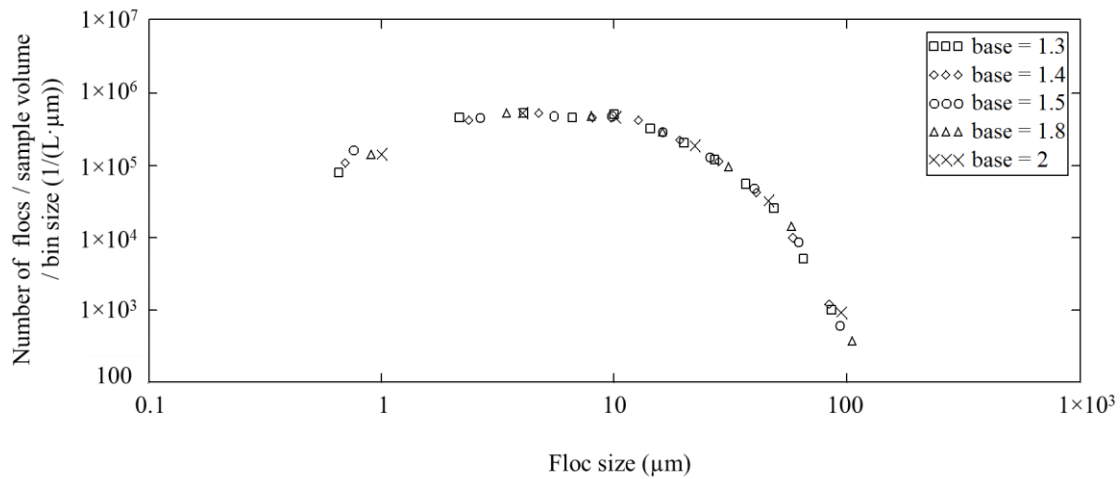
685

686 **Figure 16. Floc size distributions of settled water according to different bin sizes (PACl**
 687 **dose = 0.53 mg/L as Al).**

688 The horizontal axis in Figure 16 is the spherical-equivalent floc diameter while the vertical axis
 689 is the total number of flocs per sample volume per bin size within each floc size range. For each
 690 set of data, bin size was varied in a power law relation to a base. For instance, when the base is
 691 selected to be 1.3, the size of the first bin would be 1.3 μm and the first bin is defined by a lower
 692 bound of 0 μm and an upper bound of 1.3 μm , the second bin size is $1.3^2 \mu\text{m}$ ($=1.7 \mu\text{m}$) and the
 693 lower and upper bounds are 1.3 μm and 3.0 μm . The third bin is $1.3^3 \mu\text{m}$ ($=2.2 \mu\text{m}$) and its lower
 694 and upper bounds are 3.0 μm and 5.2 μm , and so on. The median value of each bin is considered
 695 as the mean diameter of flocs for that size range. The number of flocs within each bin was then
 696 counted by the LabVIEW histogram function.

697 For alternative bases, there were only slight changes in the shape of the distribution curve and
 698 the area under the curve. This result indicates that the specification of bin size over the range
 699 tested had little impact on the particle size distribution curve.

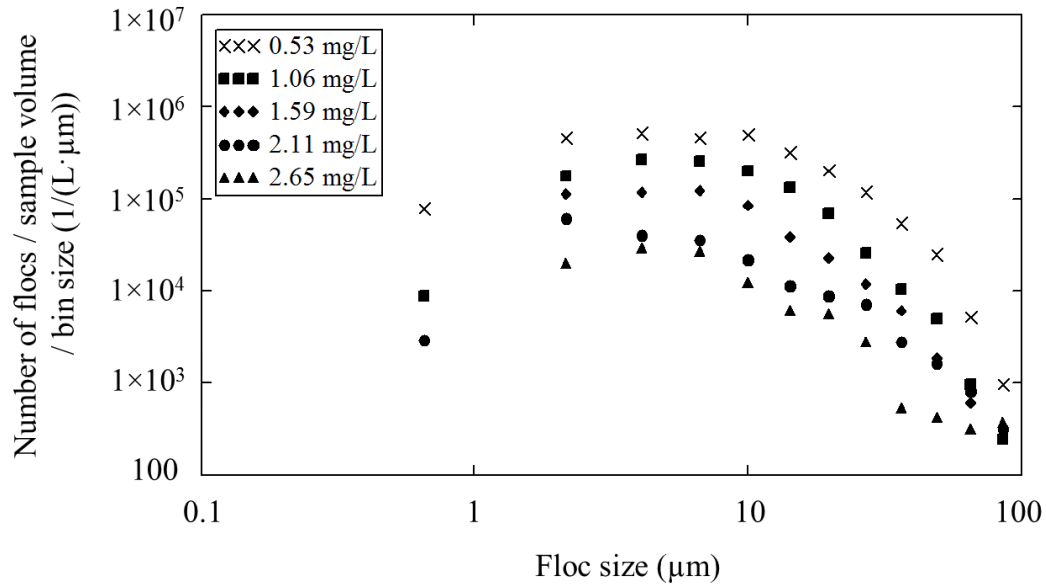
700 Figure 17 shows a log-log plot of the floc number concentration versus size. The bin sizes for
701 each base were determined as described above. The changes in bin sizes had little influence on
702 the log-log plot of floc size distribution.



703

704 **Figure 17. Log-log plot of floc size distributions of settled water according to different bin**
705 **sizes (PACl dose = 0.53 mg/L as Al).**

706 Figure 18 indicates that the number concentration of flocs in the settled water decreased with the
707 increase in PACl dose. As is shown in Figure 9, the largest floc predicted to escape the tube
708 settler at a capture velocity of 0.21 mm/s is 120 µm. As seen in Figure 18, the maximum floc
709 size observed in the settled water was less than 120 µm, which is in agreement with the model.



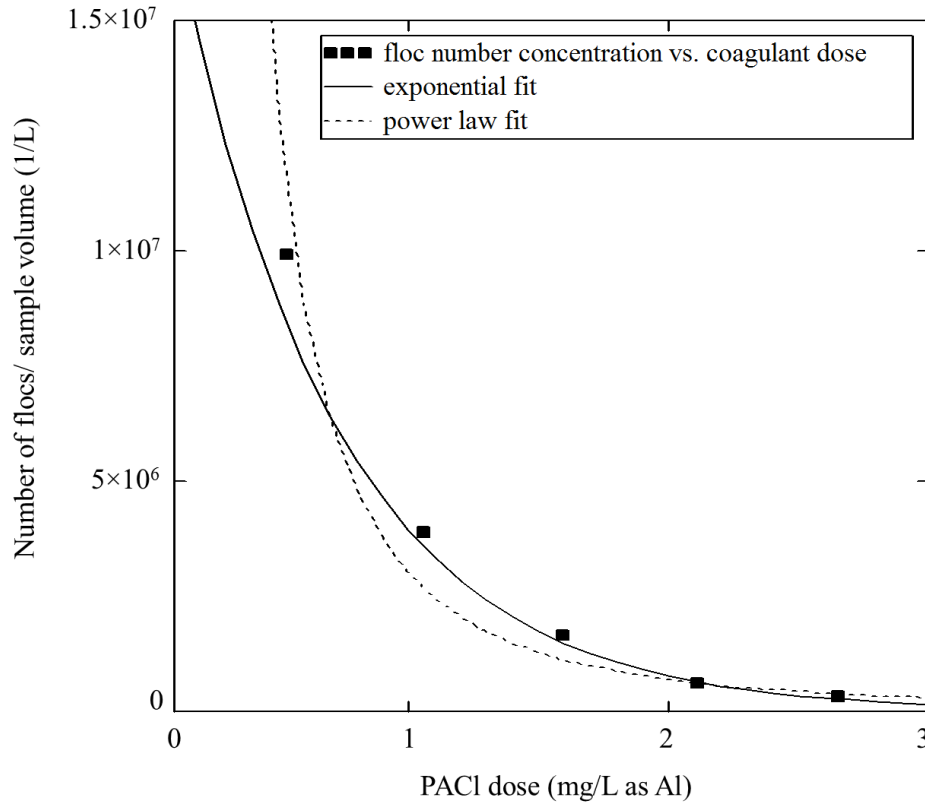
710

711 **Figure 18. Floc size distributions of settled water at different PACl dose (mg/L as Al).**

712 The data in Figure 19 suggests that the number concentration of flocs in the settled water

713 decreases as a function of coagulant dose. Both an exponential and power law provided a good

714 fit to the data in Figure 19. The fits to the data are shown in Table 4.



715

716 **Figure 19. Floc number concentration in the settled water versus PACl dose (mg/L as Al).**

717 At low coagulant doses, pC^* had a linear relationship with the logarithm of PACl dose,
 718 indicating that turbidity and coagulant dose followed a power law relation (see Figure 15). The
 719 sum of squared errors of prediction (SSE) of exponential fit was lower than that of power law fit
 720 (see Table 4). However, it was difficult to conclude which regression better fit the data in Figure
 721 19 because both the r squared values shown in Table 4 were quite high. Further studies over a
 722 wider range of coagulant doses (coagulant doses less than 1 mg/L as Al) should be conducted to
 723 see how floc number concentration is reduced as a function of coagulant dose.

724

725

726

727

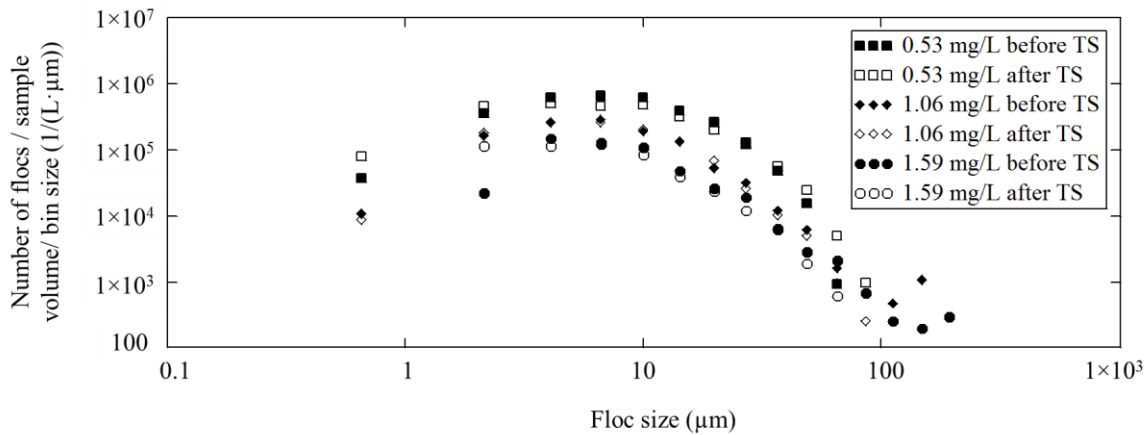
Table 4. Exponential fit and power law fit in Figure 19.

Trend line option	Trend line equation	r ²	SSE
Exponential fit	$y = 2 \times 10^7 e^{-1.6x} \frac{1}{L}$	1.00	2.3×10^{12}
Power law fit	$y = 3 \times 10^6 x^{-2.1} \frac{1}{L}$	0.96	4.1×10^{12}

728

729 2.6.3 Comparison between flocculated water and settled water

730 In Figure 20, floc size distributions are compared between flocculated water and settled water to
 731 evaluate the performance of the tube settler. Flocculated water was sampled after the flocculator,
 732 while settled water was sampled after the tube settler.



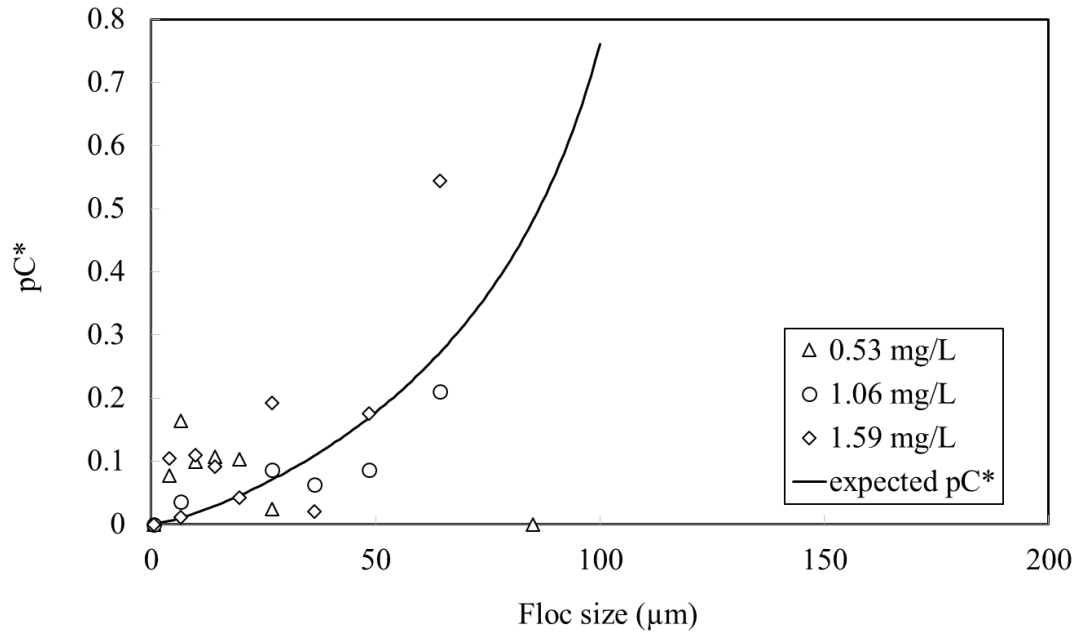
733

734 **Figure 20. Size distributions of flocculated water and settled water at different PACl doses**
 735 **(mg/L as Al). (TS designates tube settler.)**

736 The results confirm that sedimentation does little to remove particles below the capture velocity
 737 of the sedimentation tank. One concern with the results shown in Figure 20 is that the

738 concentration of small flocs (less than 5 μm) in the settled water was higher than that in the
739 flocculated water. The inner diameter of the connecting tube between the tube settler and the
740 turbidimeter was constrained by the 0.95 cm exit port diameter of the tube settler (see Figure 22
741 in Appendix. C), thus the velocity gradient inside the connecting tube was 87/s, 24% higher than
742 that inside the flocculator. The higher shear inside the connecting tube may break big flocs into
743 small ones. However, preferential production of floc fragments smaller than 5 μm would not be
744 expected. Another explanation for the observed increase in small flocs might be overlapping of
745 flocs in the depth of field within the image volume. When there is a large floc in the image, small
746 flocs behind or in front would not be detected by image analysis. The flocculated water has more
747 large flocs (diameter greater than 70 μm) than the settled water. Therefore, the number of small
748 flocs in flocculated water is more likely to be under-estimated due to the image occlusion caused
749 by big flocs. The number concentration of flocs for each bin size could possibly be corrected for
750 occlusion by larger flocs to improve this analysis. The occluded volume would be obtained by
751 the area of the larger flocs multiplied by the calculated depth of field.

752 Figure 21 shows pC^* for the three coagulant doses as a function of floc sizes and the expected
753 pC^* based on predicted tube settler performance for the ratio of terminal velocity to capture
754 velocity.



755

756

Figure 21. pC* value versus floc size.

757

The observed concentration changes between settled water and flocculated water were negligible (pC* of less than 0.2) except for particles that approach the capture velocity of the sedimentation tank.

759

760 **2.7 Conclusions**

761

This paper presents an effective way to employ digital image analysis to continuously count and size flocs in a flow-through-cell. Out-of focus particles are automatically identified and excluded thus improving the accuracy of the results of floc size measurement. The constraints for floc size measurements are the field of view, the depth of field and the airy patterns caused by the objective lens. The apparatus could measure particle sizes ranging from around 2.6 μm to more than 300 μm. The error in measuring particle sizes caused by airy disk (light diffraction) was

766

767 measured by testing particles of known diameter. The influence of airy disk accounted for a
768 correction of 2.6 μm , which was consistent with the estimated diameter of the airy disk.

769 The average particle diameter of the test suspension of kaolinite clay was measured to be
770 $7.7 \pm 3.8 \mu\text{m}$ and a linear relationship was obtained between turbidity and the concentration of
771 clay particles determined by imaging.

772 Size distribution of flocs could be plotted in varying bin sizes, when the bin sizes increased with
773 particle size following a power law. Since there are fewer large flocs, the bin size was kept
774 proportional to the bin mean diameter to ensure that sufficient flocs were in the large bins to
775 obtain a statistically meaningful particle count in each bin. Thus, varying the bin size with floc
776 diameter can better reveal the shape of the size distribution curve. The shape and the area under
777 the size distribution curves were independent of the bases used to set bin size.

778 For settled water, as was expected, floc number concentrations decreased when the PACl dose
779 increased. pC^* had a linear relationship with the logarithm of PACl dose. The maximum floc
780 size observed in the effluent was less than 120 μm , which was in accordance with the value
781 predicted by a model for the capture velocity of the experimental tube settler. Image occlusion
782 caused by overlapping flocs may result in the underestimation of the number concentration of
783 small flocs in flocculated water.

784 Image analysis of flocculated water could be used to predict particle counts after sedimentation.
785 This has the potential to be used to improve performance of water treatment plants especially
786 during raw water quality changes.

787 **2.8 Future work**

788 The value of α_t and β_t were determined based on looking at a range of computed α and β from
789 large sets of floc images. The determination of α_t and β_t may be influenced by the floc image
790 sample size (the number of floc images taken from the sample cell). In addition, the sample size
791 may also affect the particle size distribution curve during flocculation. The study of the effect of
792 variances in sample sizes on particle size distribution could improve the analysis.

793 At low coagulant doses, pC^* had a linear relationship with the logarithm of PACl dose,
794 indicating that turbidity and coagulant dose followed a power law relation. However, the
795 relationship between floc concentration in the settled water and coagulant dose was less
796 apparent. Both exponential and power law regressions fit the data well. In future experiments, a
797 wider range of coagulant doses (coagulant doses less than 1 mg/L as Al) could be applied to the
798 flocculator to check how floc number concentration is reduced as a function of coagulant dose.

799 The floc size distribution may follow a power law relation, $N(d) \sim d^{-p}$, where $N(d)$ is the number
800 of flocs per sample volume within the diameter range of d to $d+\Delta d$. The slope ($-p$) of the particle
801 size distribution can vary depending on coagulation mechanisms, such as Brownian motion, fluid
802 shear and differential sedimentation. The observations of particle size distributions in natural
803 water sources indicate that the collision mechanisms of small (less than 2 μm) and median
804 particles (2~60 μm) are dominated by Brownian motion and fluid shear respectively, while big
805 flocs (greater than 60 μm) might be formed as a result of differential sedimentation (Li, et al.,
806 2004). Thus, the change of the slopes in the floc size distribution may indicate different
807 flocculation mechanisms for different size of particles. Future study on the slope changes may

808 improve our understanding of the interaction mechanisms between colloids as well as predict the
809 evolution of floc size distribution under different operation conditions.

810 **2.9 References**

811 Adachi, Y., and Tanaka, Y. (1997). Settling velocity of an aluminum-kaolinite floc. *Water Res.*,
812 31(3), 449-454.

813 Adelman, M. J., Hurst, M. W., Weber-Shirk, M. L., Cabrito, T. S., Somogyi, C., and Lion, L. W.
814 (2013). Floc Roll-up and its implications for the spacing of inclined settling devices.
815 *Environ. Eng. Sci.*, 30(6), 302-310.

816 Aroke, U. O., El-Nafaty, U. A., and Osha, O. A. (2013). Properties and characterization of
817 Kaolin clay from Alkaleri, north-eastern Nigeria. *IJETAE.*, 3(11), 387-392.

818 Boadway, J. D. (1978). *J. Environ. Eng.-ASCE*, 104, 901-915.

819 Bouyer, D., Coufort, C., Line, A., and Do-Quang, Z. (2004). Experimental Analysis of floc size
820 distribution under different hydrodynamics in a mixing tank. *AIChE. J.*, 50(9), 2064-2081.

821 Camp, T. R., and Stein, P. C. (1943). Velocity gradients and internal work in fluid motion. *J.*
822 *Boston Soc. Civ. Eng.*, 30, 219.

823 Chakraborti, R. K., Atkinson, J. F., and Benschoten, J. E. V. (2000). Characterization of Alum
824 Floc by Image Analysis. *Environ. Sci. Technol.*, 34(18), 3969-3976.

825 Coufort, C., Dumas, C., Bouyer, D., and Line, A. (2008). Analysis of floc size distribution in a
826 mixing tank. *Chem. Eng. Process*, 47(3), 287-294.

827 Gibbs, R. J. (1982). Floc breakage during HIAC light-blocking analysis. *Environ. Sci. Technol.*,
828 16(5), 298-299.

829 Gregory, J. (1981). Flocculation in laminar tube flow. *Chem. Eng. Sci.*, 36(11), 1789-1794.

830 Greivenkamp, J. E. (2004). *Field Guide to Geometrical Optics*. Bellingham, WA: SPIE Press.

831 Hopkins, D. C., and Ducoste, J. J. (2003). Characterizing flocculation under heterogeneous
832 turbulence. *J. Colloid. Interf. Sci.*, 264(1), 184-194.

833 “Image analysis and processing.” (2008). <www.ni.com/white-paper/3470/en/#toc2> (Jul.4,
834 2015).

835 Jiang, Q., and Logan, B. E. (1991). Fractal dimensions of aggregates determined from steady-
836 state size distributions. *Environ. Sci. Technol.*, 25(12), 2031-2038.

837 Keyvani, A., and Strom, K. (2013). A fully-automated image processing technique to improve
838 measurement of suspended particles and flocs by removing out-of-focus objects. *Comput.*
839 *Geosci.*, 52, 189-198.

840 Klinger, T. (2003). *Image Processing with LabVIEW and IMAQ Vision*. Upper Saddle River,
841 New Jersey: Pearson Education, Inc., 162-171.

842 Li, D., and Ganczarczyk, J. (1989). Fractal Geometry of Particle Aggregates Generated in water
843 and wastewater treatment processes. *Environ. Sci. Technol.*, 23(11), 1385-1389.

844 Li, T., Zhu, Z., Wang, D., Yao, C., and Tang, H. (2006). Characterization of floc size, strength
845 and structure under various coagulation mechanisms. *Powder. Technol.*, 168(2), 104-110.

846 Li, X., Zhang, J., and Lee, J. (2004). Modelling particle size distribution dynamics in marine
847 waters. *Water Res.*, 38(5), 1305-1317.

848 Matsuo, T., and Unno, H. (1981). Forces acting on floc and strength of floc. *J. Env. Eng.-ASCE*,
849 107(3), 527-545.

850 Meakin, P. (1998). *Fractals, Scaling and Growth Far From Equilibrium*. Cambridge: Cambridge
851 Univ. Press.

852 Nan, J., He, W., Song, X., and Lu, G. (2009). Impact of dynamic distribution of floc particles on
853 flocculation effect. *J. Environ. Sci.*, 21(8), 1059-1065.

854 Pal, G., and Pal, P. (2001). *Textbook of Practical Physiology* (1st ed.). Chennai: Orient
855 Blackswan. 387.

856 Parker, D. S., Kaufman, W. J., and Jenkins, D. (1972). Floc break-up in turbulent flocculation
857 processes. *J. Sanit. Eng. Div. ASCE*, 98(1), 79-99.

858 Pfitzner, J. (1976). Poiseuille and his law. *Anaesthesia*, 31(2), 273-275.

859 Swetland, K. A., Weber-Shirk, M. L., and Lion, L. W. (2014). Flocculation-Sedimentation
860 performance model for laminar-flow hydraulic flocculation with polyaluminum chloride
861 and aluminum sulfate coagulants. *J. Environ. Eng.-ASCE*, 140(3), 04014002.

862 Tambo, N., and Watanabe, Y. (1979). Physical characteristics of flocs-I. The floc density
863 function and aluminium floc. *Water Res.*, 13(5), 409-419.

864 “Thresholding.” (2013). <[http://zone.ni.com/reference/en-XX/help/372916P-](http://zone.ni.com/reference/en-XX/help/372916P-01/nivisionconcepts/thresholding/)
865 [01/nivisionconcepts/thresholding/](http://zone.ni.com/reference/en-XX/help/372916P-01/nivisionconcepts/thresholding/)> (Jul.4, 2015).

866 Tse, I. C., Swetland, K., Weber-Shirk, M. L., and Lion, L. W. (2011). Fluid shear influences on
867 the performance of hydraulic flocculation systems. *Water Res.*, 45(17), 5412-5418.

868 Vahedi, A., and Gorczyca, B. (2011). Application of fractal dimensions to study the structure of
869 flocs formed in lime softening process. *Water Res.*, 45 (2), 545-556.

870 “Wavelength effects on performance.” (2015). <[http://www.edmundoptics.com/technical-](http://www.edmundoptics.com/technical-resources-center/imaging/wavelength-effects-on-performance/)
871 [resources-center/imaging/wavelength-effects-on-performance/](http://www.edmundoptics.com/technical-resources-center/imaging/wavelength-effects-on-performance/)> (Jul. 14, 2015).

872 Weber-Shirk, M. L. (2008). “An automated method for testing process parameters.”
873 <<http://confluence.cornell.edu/display/AGUACLARA/Process+Controller+Background>>
874 (Jul. 4, 2015).

875 Wei, N., Zhang, Z., Liu, D., Wu, Y., Wang, J., and Wang, Q. (2015). Coagulation behavior of
876 polyaluminum chloride: Effects of pH and coagulant dosage. *Chinese J. Chem. Eng.*, 23(6),
877 1041-1046.

878 Xiao, F., Lam, K. M., Li, X. L., Zhong, R. S., and Zhang, X. H. (2011). PIV characterization of
879 flocculation dynamics and floc structure in water treatment. *Colloid. Surface. A.*, 379(1-3),
880 27-35.

881 Yao, M., Nan, J., and Chen, T. (2014). Effect of particle size distribution on turbidity under
882 various water quality levels during flocculation processes. *Desalination*, 354, 116-124.

883 Zhang, Z., Zhao, J., Xia, S., Liu, C., and Kang, X. (2007). Particle size distribution and removal
884 by a chemical-biological flocculation process. *J. Environ. Sci.*, 19(5), 559-563.

885

886

APPENDIX

887 **A. Calculation of \bar{G} , Q, L**

888 Under laminar flow conditions (i.e. when the Reynolds number, $Re \leq 2100$), the velocity of fluid
889 at a radial distance r from the pipe axis, through a straight pipe with a circular cross section, can
890 be expressed by equation (12) (Gregory, 1981),

$$891 \quad v_r = v_0 \left(1 - \frac{r^2}{R^2}\right) \quad (12)$$

892 where, v_r is the velocity of fluid at a radial distance r from the pipe axis,

893 v_0 is the maximum velocity in the fluid (the axis velocity),

894 r is the radial distance from the pipe axis,

895 R is the radius of the pipe.

896 The average velocity of the fluid can be obtained by integrating Equation (12),

$$897 \quad \bar{v} = \frac{\int_0^R v_0 \left(1 - \frac{r^2}{R^2}\right) 2\pi r dr}{\int_0^R 2\pi r dr} = \frac{v_0}{2} \quad (13)$$

898 Gregory (1981) argued that the velocity gradient G at a radial distance from the pipe axis could
899 be defined by differentiation of equation (12),

$$900 \quad G = \frac{dv_r}{dr} = 2v_0 r / R^2 \quad (14)$$

901 G increases from zero at the pipe axis to a maximum value at the wall.

902 The average velocity gradient in the pipe can then be calculated as,

$$903 \quad \bar{G} = \frac{2v_0 \int_0^R 2\pi r^2 dr}{R^2 \int_0^R 2\pi r dr} = \frac{4v_0}{3R} \quad (15)$$

$$904 \quad \text{Since } Q = \frac{v_0}{2} \pi R^2, \quad (16)$$

$$905 \quad \bar{G}_{Gregory} = \frac{8}{3} \frac{Q}{\pi R^3} = \frac{64}{3} \frac{Q}{\pi D^3} \quad (17)$$

906 Camp and Stein (1943) suggested that the average velocity gradient could be obtained from the
907 power input to the volume of the pipe:

$$908 \quad \bar{G} = \sqrt{\frac{P}{\mu V}} \quad (18)$$

909 Where, P is the power input of the system,

910 μ is the dynamic viscosity of the fluid,

911 V is the volume of the pipe.

912 The power input of the system could be expressed as the product of the flow rate and the
913 pressure drop across the tube,

$$914 \quad P = Q\Delta p \quad (19)$$

915 For a long cylindrical pipe, the Hagen-Poiseuille law (Pfitzner, 1976) leads to the calculation of
916 the pressure drop across the pipe.

$$917 \quad \Delta p = \frac{128Q\mu L_{tube}}{\pi D^4} \quad (20)$$

918 Where, L_{tube} is the length of the flocculator tube.

919 Combing equation (18), (19), (20) and considering $V = \pi R^2 L$, the Camp Stein expression of
920 average G can be represented by:

$$921 \quad \overline{G_{CampStein}} = \frac{16\sqrt{2}Q}{\pi D^3} \quad (21)$$

922 For the experimental conditions, the average velocity gradient calculated by Camp Stein
923 (70.57/s) is 6% higher than that from Gregory.

924 The energy dissipation rate used in this research was: $\varepsilon = 5 \frac{mW}{kg}$. The velocity gradient can be
925 calculated by equation (1) and (2) and thus the estimated average G would be $70.6s^{-1}$. A range
926 of Q values were substituted into equation (2) to obtain the desired experimental velocity
927 gradient. At $Q_{plant} = 215 \frac{mL}{min}$, $G = 70.6 s^{-1}$. When $G\theta$ is greater than 20,000, it is expected that
928 there would be successful flocculation in the flocculator (Camp and Stein, 1943). For safety, a
929 $G\theta$ value of 21,000 was selected. Hence, the residence time and the length of the tube could be
930 separately calculated by equation (22) and equation (23), where A_{Tube} is the cross sectional area
931 of the tube.

$$932 \quad \theta = \frac{21000}{G} \quad (22)$$

$$933 \quad L_{tube} = \theta \frac{Q}{A_{tube}} \quad (23)$$

934 The resulting residence time of the flocculator was 300 s and the length of the tube was 49 ft.

935 **B. Flow rate, coagulant dose and influent turbidity**

936 The constraints of the flow rate through the apparatus were the minimum flow rates required for
937 the turbidity meter and the maximum rate for the flow cell. A flow rate of 3.58 ml/s through the
938 apparatus met the minimum 1.67 ml/s requirement for the turbidity meter.

939 The flow rate needed for the coagulant solution was calculated by the law of conservation of
940 mass.

$$941 \quad Q_{Al} = Q_{plant} \times \frac{C_{plant}}{C_{Al}} \quad (24)$$

942 Where, Q_{Al} is the flow rate of coagulant solution,

943 Q_{plant} is the flow rate through the flocculator,

944 C_{plant} is the Al dose within the flocculator,

945 C_{Al} is the Al concentration of coagulant stock.

946 Equation (25) was used to calculate the concentration of clay added to water, the value of

947 $1.73 \frac{mg}{L \cdot NTU}$ was measured in the lab by Casey Garland (personal communication, June 13, 2015).

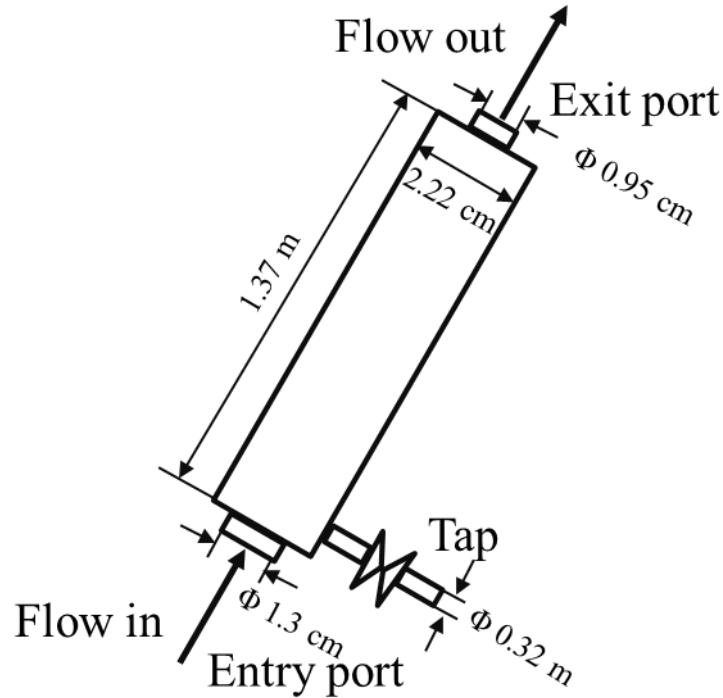
$$948 \quad C_{clay} = 1.73 \frac{mg}{L \cdot NTU} \cdot Target \ NTU \quad (25)$$

949 **C. Tube settler**

950 The 1.37 m (4.5 ft) tube settler (whose inner cross sectional dimensions are 2.22 cm×2.22 cm)

951 has an entry port diameter of 1.3 cm (½ in) near the bottom and an exit port diameter of 0.95 cm

952 (3/8 in) near the top, as is shown in Figure 22. A 0.32 cm (1/8 in) diameter tap, is located on the
 953 end near to the bottom. The tap is used as a drain to remove flocs.



954

955

Figure 22. Tube settler.

956 The tube settler capture velocity was determined by following equation v_{up} is the vertical
 957 component of the velocity in the setting tube ($v_{tube settler}$) and $v_{capture}$ is the capture velocity. θ
 958 is the angle of the tube settler and S is the inner width of the tube settler. $L_{tube settler}$ is the
 959 length of tube settler.

960
$$v_{up} = v_{tube settler} \cdot \sin \theta \tag{26}$$

961
$$v_{capture} = \frac{v_{up} \cdot S}{L_{tube settler} \cdot \cos \theta \cdot \sin \theta + S} \tag{27}$$

962 **D. Number concentration of primary particles**

963 The number of primary particles in each floc was calculated by the following equation,

$$964 \quad n_i = \left(\frac{d}{d_{clay}} \right)^{D_{fractal}} \quad (28)$$

965 The total number of primary particles within sample volume can be obtained from,

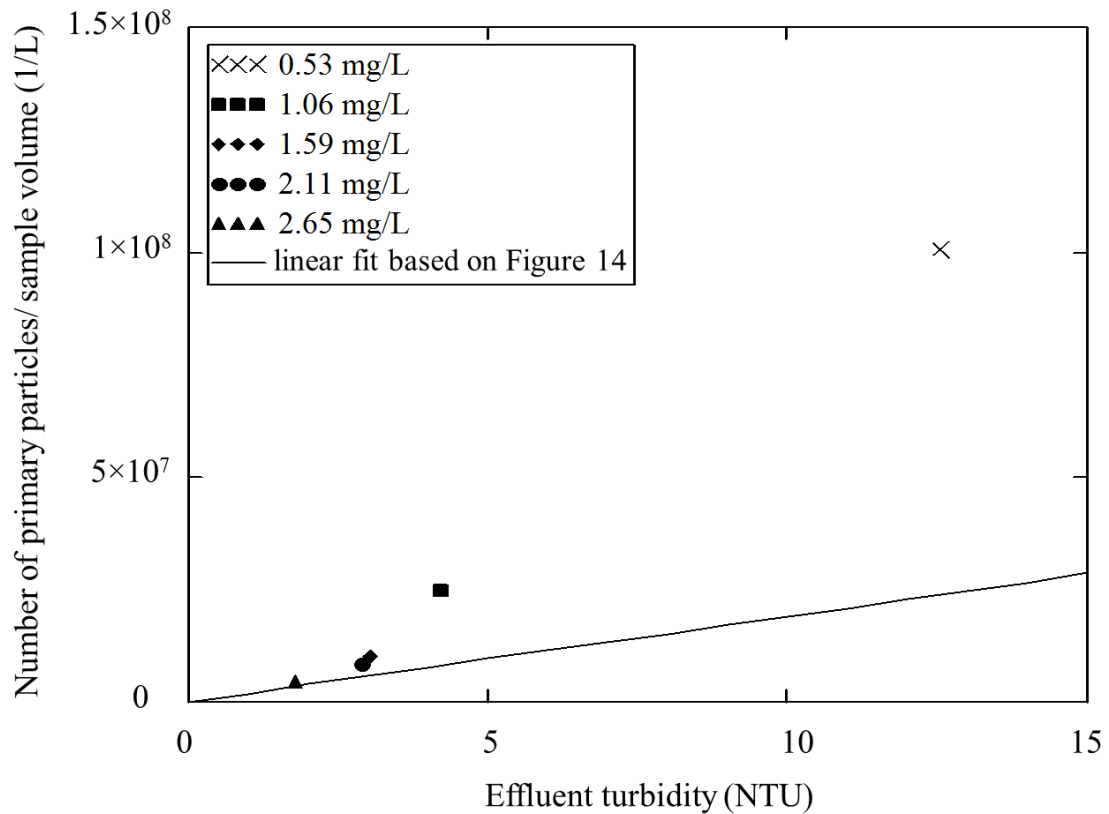
$$966 \quad n_{total} = \sum_{i=1}^k n_i \quad (29)$$

967 Where n_i is the number of primary particles in floc i ,

968 k is the total number of flocs and $D_{fractal}$ was assumed to have the value of 2.3 reported
969 by Li and Ganczarczyk (1989).

970 Figure 23 shows the estimated number of primary particles per sample volume in the effluent for
971 each PACl dose (mg/L as Al). The straight line in the graph is the zero-intercept linear fit
972 determined in Figure 14, which was used to predict the number of clay particles per sample
973 volume at a given effluent turbidity. Turbidity of flocculated water was measured and turned out
974 to be almost the same as the turbidity of raw clay water (without coagulants). Hence, the
975 expectation was that turbidity would be related to the concentration of primary particles,
976 meaning data points in Figure 23 should fit the relationship determined for unflocculated clay
977 suspensions.

$$978 \quad Turbidity \sim n_{total} \quad (30)$$



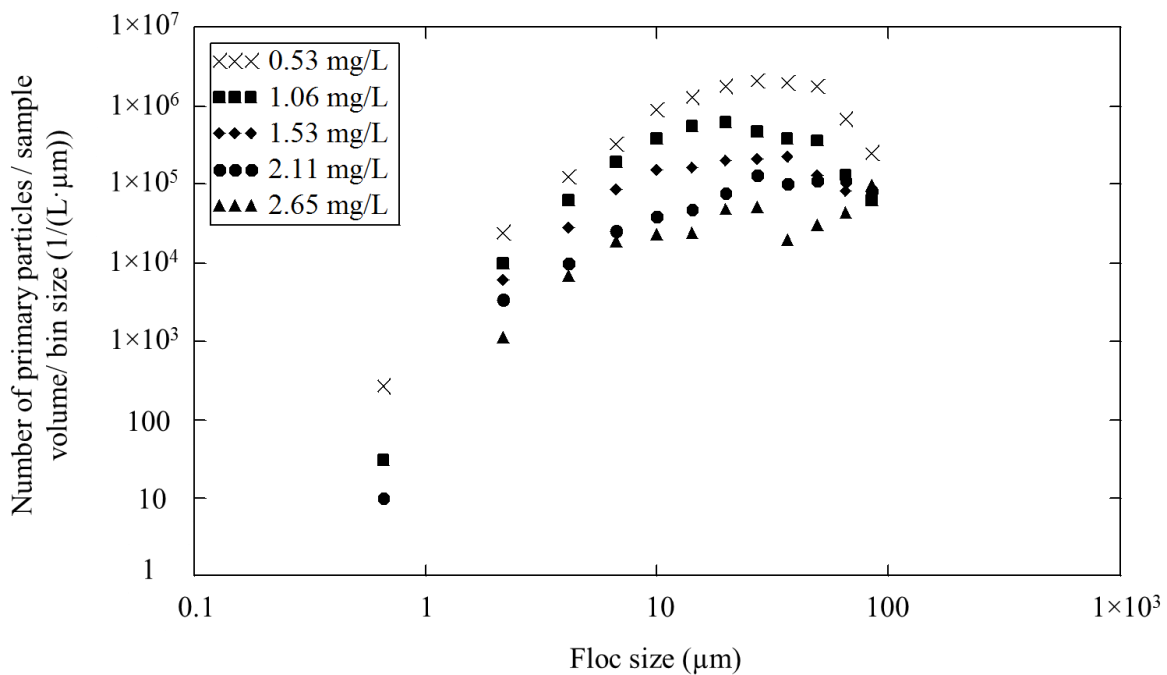
979

980 **Figure 23. Estimated number of primary particles in the effluent at different aluminum**
 981 **doses based on an assumed fractal dimension of 2.3. Solid line is fit of number of particles**
 982 **per NTU based on Figure 14.**

983 Figure 23 shows estimated primary particle number concentrations far exceeded the model. One
 984 possible explanation is that the fractal dimension of 2.3 assumed here might be incorrect. In
 985 addition, the fractal dimension can change under hydrodynamic (Li, et al., 2006) or
 986 physicochemical (Xiao, et al., 2011) conditions and has a wide range. As noted above, the
 987 reported 3-D fractal dimension of flocs have a range from 1.6 to 2.3 (Li and Ganczarczyk, 1989).
 988 Due to the power law relation, an increase in fractal dimension would result in a rapid increase in
 989 primary particle numbers.

990 The relationship between turbidity and primary particle number concentrations in flocs was less
 991 apparent, perhaps due to the assumption of an incorrect fractal dimension value. Further studies
 992 should be conducted on the determination of 3-D fractal dimension from 2-D floc images. This
 993 relationship will enable prediction of turbidity based on image analysis.

994 Figure 24 indicates that the number concentration of primary particles in the settled water
 995 decreased with the increase in PACl dose. Flocs ranging from 20 to 50 μm in diameter accounted
 996 for the greatest proportion of the primary particle concentration.



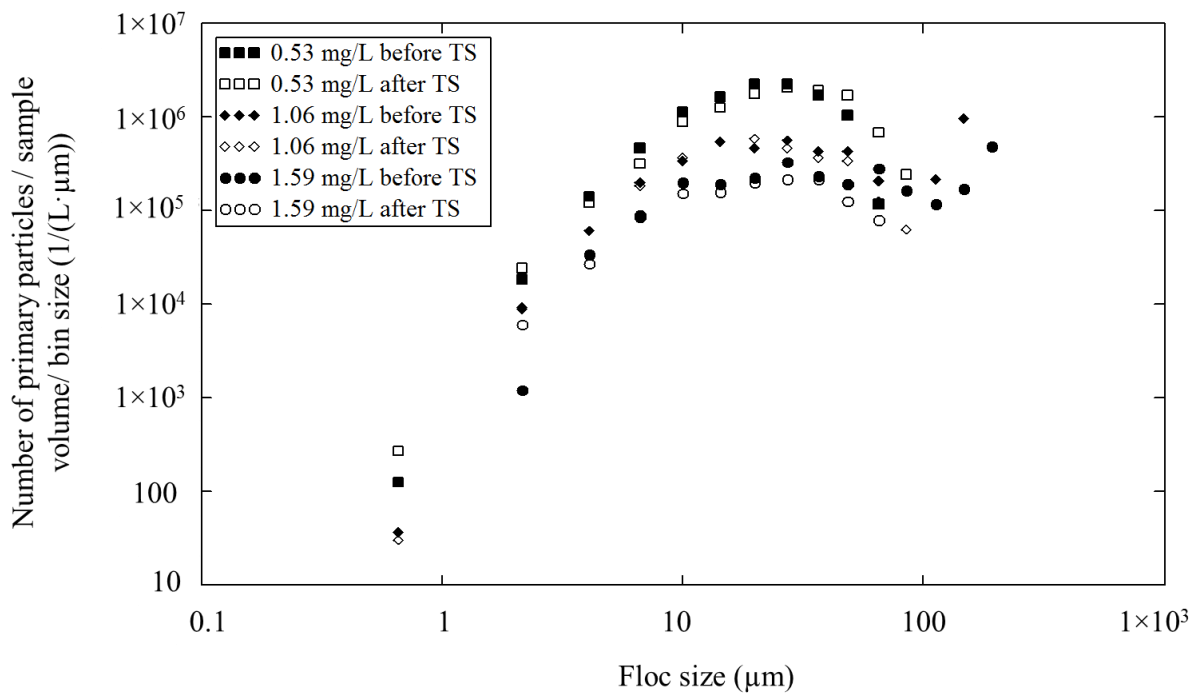
997

998 **Figure 24. Primary particle distribution in the settled water at different PACl dose (mg/L**
 999 **as Al).**

1000 As illustrated in Figure 10, the experimental tube settler can achieve 100% removal of flocs
 1001 greater than 120 μm while flocs around 68 μm would be expected to be removed with 50%
 1002 efficiency in the tube settler. Thus, big flocs (greater than 70 μm) occupied a small proportion of

1003 the mass due to their high removal efficiency. Flocs less than 10 μm account for less mass
 1004 perhaps as a consequence of flocculation.
 1005 Primary particle distributions were compared between flocculated water and settled water
 1006 to evaluate the performance of the tube settler in Figure 25. The concern in Figure 25 is the same
 1007 as the one in Figure 20, as was mentioned in part 2.6.3.

1008



1009

1010 **Figure 25. Primary particle distribution of flocculated water and settled water at different**
 1011 **PACl doses (mg/L as Al). (TS designates tube settler.)**

1012 **E. Fractal dimension**

1013 Fractal dimension is a crucial parameter in determining the floc shape, density, porosity, and
 1014 settling velocity, as well as their kinematic behaviors, such as particle aggregation and breakup.

1015 Numerous ways have been suggested to calculate the 3D fractal dimension. These ways include
1016 direct methods, such as a box-counting method (Vahedi and Gorczyca, 2011), and indirect
1017 methods, like a free settling test. One of the direct methods to determine the three-dimensional
1018 fractal dimension will be discussed here. This method is to relate the number of primary particles
1019 to the floc diameter (Meakin, 1998),

$$1020 \quad d = d_{clay} n_i^{\frac{1}{D_{fractal}}} \quad (31)$$

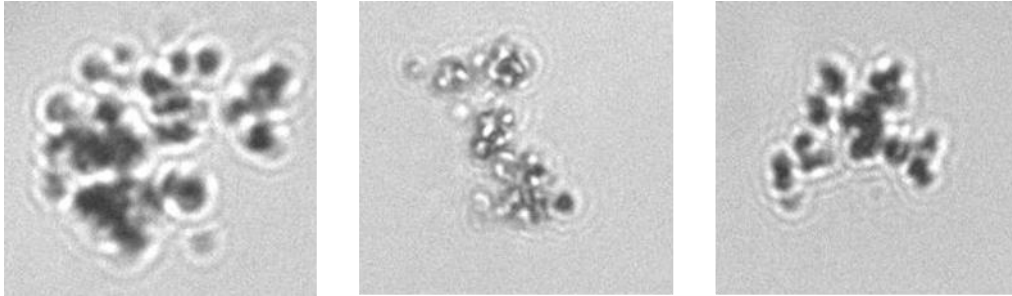
1021 The number of primary clay particles in 3D dimension (n_i) could be estimated from the number
1022 of clay particles in the 2D image (n_0), based on the assumption that the flocs were spherical.
1023 Thus, the total number of primary particles in 3D dimension would be

$$1024 \quad n_i = \frac{4}{3} \pi \left(\sqrt{\frac{n_0}{\pi}} \right)^3 \quad (32)$$

1025 Where, n_0 is the number of primary particles counted in a 2D image.

1026 The fractal dimension could be then calculated by the power law fitting of equation (31).

1027 Figure 26 shows several sample images of flocs. In terms of equation (32), the number of
1028 primary particles was counted to determine the fractal dimension of flocs. Using the graphs in
1029 Figure 26 for illustration, there were approximately twenty clay particles in the first floc. The
1030 second and third floc images have 22 and 15 clays each.



1031

1032

Figure 26. Sample images of flocs.

1033

After regression analysis, the power in Figure 27 was calculated as 0.53. The 3D fractal

1034

dimension was calculated according to equation (31) and the result was approximately 1.9,

1035

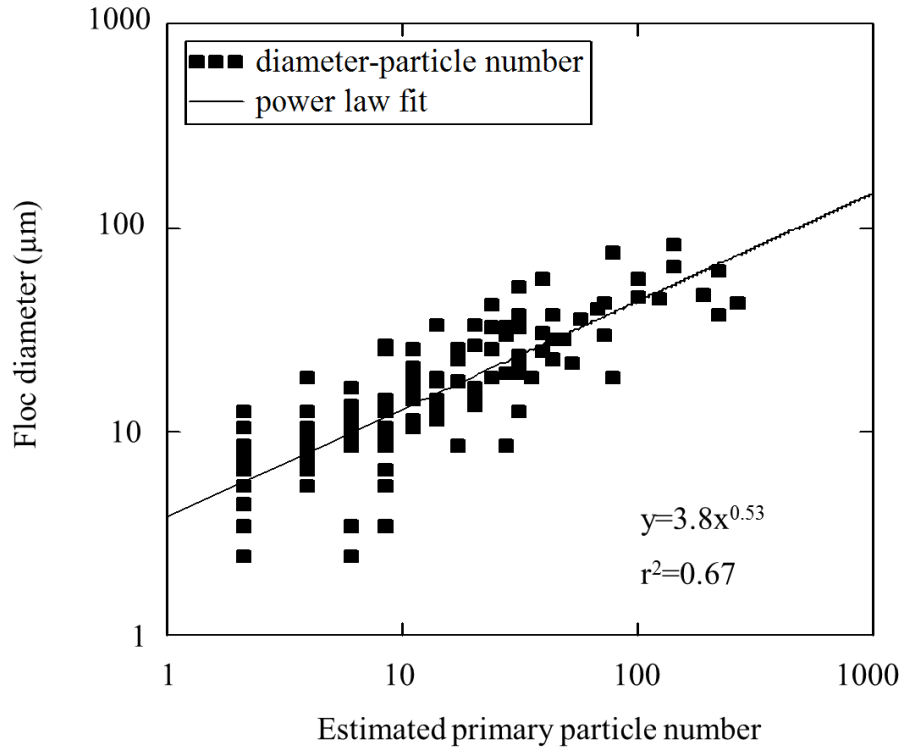
which was within the range of 1.6~2.3 indicated by Li and Ganczarayk's (1989) result. The

1036

constraint of this method is that it could only count the clay number in flocs smaller than 50 μm .

1037

For flocs larger than 50 μm , the aggregates were too densely packed to count.



1038

1039 **Figure 27. The regression of floc diameter vs. estimated primary particle numbers.**

1040 Maggi (2007) proposed another way to calculate perimeter-based fractal dimension. It is
 1041 calculated to compare with the 3D fractal dimension attained by the power law fit of equation
 1042 (31).

1043 In Maggi's theory, the 2D fractal dimension is defined as

$$1044 \quad D_p = 2 \frac{\log P_{pixel}}{\log A_{pixel}} \quad (33)$$

1045 Where P_{pixel} is the perimeter of the floc while A is the projected area of the floc. Both P_{pixel} and
 1046 A_{pixel} are in units of pixels. D_p ranges from 1~2. The 3D volume fractal dimension D_v can
 1047 then be derived from D_p when D_p is smaller than 2.

1048
$$D_v = \sqrt{\frac{a(x)}{D_p - b(x)}} \quad (34)$$

1049 Where $x = \frac{d}{l_{pixel}}$, is the dimensionless floc size, d is the floc diameter and l_{pixel} is the pixel size.

1050 $a(x)$ and $b(x)$ are used to take the resolution into account and can be calculated from the

1051 following equations,

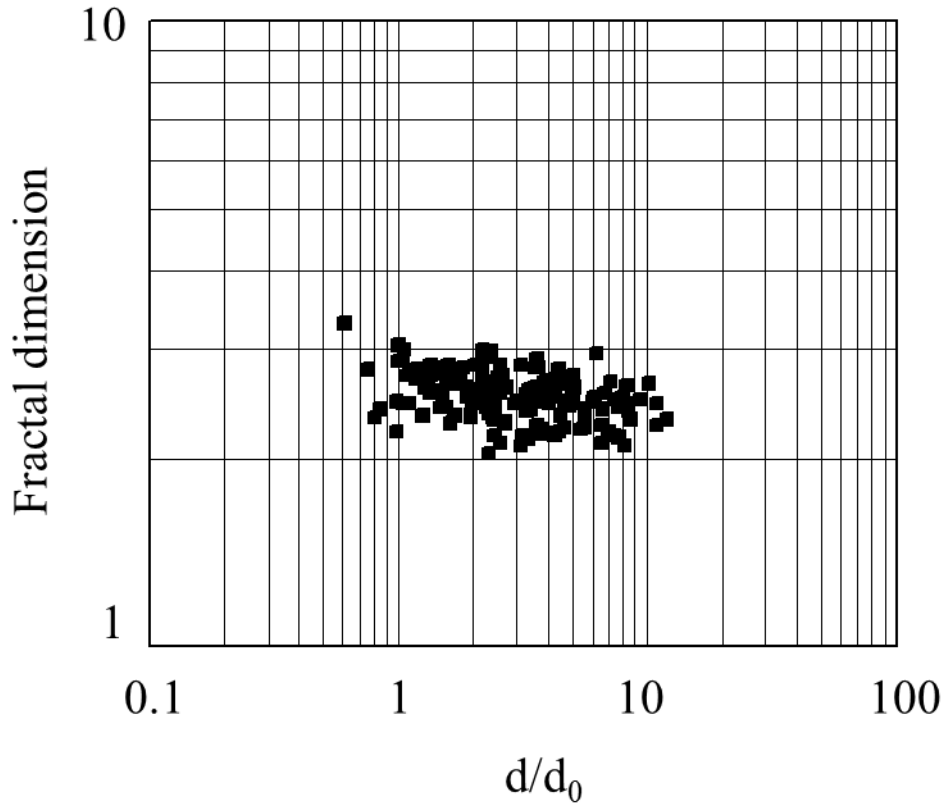
1052
$$a(x) = 9[z(x) - b(x)] \quad (35)$$

1053
$$b(x) = \frac{2[k(x)^2] - 9z(x)}{[k(x)^2] - 9} \quad (36)$$

1054 Where $k(x) = z(x)[z(x) - 1] + 1 \quad (37)$

1055
$$z(x) = \frac{\log(4x-4)}{\log x} \quad (38)$$

1056 Figure 28 shows the D_v calculated by equation (34).



1057

1058

Figure 28. Volume fractal dimension of flocs.

1059 The average fractal dimension value was 2.51 ± 0.22 . The fractal dimension values are presented

1060 in the double-logarithmic plot graph. The values decreased with increasing the dimensionless

1061 size d/d_0 , indicating that flocs appeared less dense and much more loosely clustered as the floc

1062 diameter increased.

1063

1064

1065

REFERENCES

- 1066
- 1067 Adachi, Y., and Tanaka, Y. (1997). Settling velocity of an aluminum-kaolinite floc. *Water Res.*,
1068 31(3), 449-454.
- 1069 Adelman, M. J., Hurst. M. W., Weber-Shirk, M. L., Cabrito, T. S., Somogyi, C., and Lion, L. W.
1070 (2013). Floc Roll-up and its implications for the spacing of inclined settling devices.
1071 *Environ. Eng. Sci.*, 30(6), 302-310.
- 1072 AguaClara. 2015. “AguaClara Plants.” < <http://aguaclara.cee.cornell.edu/about/projectmap/>>
1073 (Jul. 7, 2015).
- 1074 Aroke, U. O., El-Nafaty, U. A., and Osha, O. A. (2013). Properties and characterization of
1075 Kaolin clay from Alkaleri, north-eastern Nigeria. *IJETAE.*, 3(11), 387-392.
- 1076 Boadway, J. D. (1978). *J. Environ. Eng.-ASCE*, 104, 901-915.
- 1077 Bouyer, D., Coufort, C., Line, A., and Do-Quang, Z. (2004). Experimental Analysis of floc size
1078 distribution under different hydrodynamics in a mixing tank. *AIChE. J.*, 50(9), 2064-2081.
- 1079 Camp, T. R., and Stein, P. C. (1943). Velocity gradients and internal work in fluid motion. *J.*
1080 *Boston Soc. Civ. Eng.*, 30, 219.
- 1081 Chakraborti, R. K., Atkinson, J. F., and Benschoten, J. E. V. (2000). Characterization of Alum
1082 Floc by Image Analysis. *Environ. Sci. Technol.*, 34(18), 3969-3976.

1083 Coufort, C., Dumas, C., Bouyer, D., and Line, A. (2008). Analysis of floc size distribution in a
1084 mixing tank. *Chem. Eng. Process*, 47(3), 287-294.

1085 Gibbs, R. J. (1982). Floc breakage during HIAC light-blocking analysis. *Environ. Sci. Technol.*,
1086 16(5), 298-299.

1087 Gregory, J. (1981). Flocculation in laminar tube flow. *Chem. Eng. Sci.*, 36(11), 1789-1794.

1088 Greivenkamp, J. E. (2004). *Field Guide to Geometrical Optics*. Bellingham, WA: SPIE Press.

1089 Hopkins, D. C., and Ducoste, J. J. (2003). Characterizing flocculation under heterogeneous
1090 turbulence. *J. Colloid. Interf. Sci.*, 264(1), 184-194.

1091 “Image analysis and processing.” (2008). <www.ni.com/white-paper/3470/en/#toc2> (Jul.4,
1092 2015).

1093 Jiang, Q., and Logan, B. E. (1991). Fractal dimensions of aggregates determined from steady-
1094 state size distributions. *Environ. Sci. Technol.*, 25(12), 2031-2038.

1095 Keyvani, A., and Strom, K. (2013). A fully-automated image processing technique to improve
1096 measurement of suspended particles and flocs by removing out-of-focus objects. *Comput.*
1097 *Geosci.*, 52, 189-198.

1098 Klinger, T. (2003). *Image Processing with LabVIEW and IMAQ Vision*. Upper Saddle Rive,
1099 New Jersey: Pearson Education, Inc., 162-171.

1100 Li, D., and Ganczarczyk, J. (1989). Fractal Geometry of Particle Aggregates Generated in water
1101 and wastewater treatment processes. *Environ. Sci. Technol.*, 23(11), 1385-1389.

- 1102 Li, T., Zhu, Z., Wang, D., Yao, C., and Tang, H. (2006). Characterization of floc size, strength
1103 and structure under various coagulation mechanisms. *Powder. Technol.*, 168(2), 104-110.
- 1104 Li, X., Zhang, J., and Lee, J. (2004). Modelling particle size distribution dynamics in marine
1105 waters. *Water Res.*, 38(5), 1305-1317.
- 1106 Maggi, F. (2007). Variable fractal dimension: A major control for floc structure and flocculation
1107 kinematics of suspended cohesive sediment. *J. Geophys. Res.*, 112(C7).
- 1108 Matsuo, T., and Unno, H. (1981). Forces acting on floc and strength of floc. *J. Env. Eng.-ASCE*,
1109 107(3), 527-545.
- 1110 Meakin, P. (1998). *Fractals, Scaling and Growth Far From Equilibrium*. Cambridge: Cambridge
1111 Univ. Press.
- 1112 Nan, J., He, W., Song, X., and Lu, G. (2009). Impact of dynamic distribution of floc particles on
1113 flocculation effect. *J. Environ. Sci.*, 21(8), 1059-1065.
- 1114 Pal, G., and Pal, P. (2001). *Textbook of Practical Physiology* (1st ed.). Chennai: Orient
1115 Blackswan. 387. Color vision
- 1116 Parker, D. S., Kaufman, W. J., and Jenkins, D. (1972). Floc break-up in turbulent flocculation
1117 processes. *J. Sanit. Eng. Div. ASCE*, 98(1), 79-99.
- 1118 Pfitzner, J. (1976). Poiseuille and his law. *Anaesthesia*, 31(2), 273-275.
- 1119 Swetland, K. A., Weber-Shirk, M. L., and Lion, L. W. (2014). Flocculation-Sedimentation
1120 performance model for laminar-flow hydraulic flocculation with polyaluminum chloride
1121 and aluminum sulfate coagulants. *J. Environ. Eng.-ASCE*, 140(3), 04014002.

1122 Tambo, N., and Watanabe, Y. (1979). Physical characteristics of flocs-I. The floc density
1123 function and aluminium floc. *Water Res.*, 13(5), 409-419.

1124 “Thresholding.” (2013). <[http://zone.ni.com/reference/en-XX/help/372916P-](http://zone.ni.com/reference/en-XX/help/372916P-01/nivisionconcepts/thresholding/)
1125 [01/nivisionconcepts/thresholding/](http://zone.ni.com/reference/en-XX/help/372916P-01/nivisionconcepts/thresholding/)> (Jul.4, 2015).

1126 Tse, I. C., Swetland, K., Weber-Shirk, M. L., and Lion, L. W. (2011). Fluid shear influences on
1127 the performance of hydraulic flocculation systems. *Water Res.*, 45(17), 5412-5418.

1128 United Nations. (2012). “The millennium development goals report.”
1129 <<http://www.un.org/millenniumgoals/pdf/MDG%20Report%202012.pdf>> (Jul. 7, 2015).

1130 Vahedi, A., and Gorczyca, B. (2011). Application of fractal dimensions to study the structure of
1131 flocs formed in lime softening process. *Water Res.*, 45 (2), 545-556.

1132 “Wavelength effects on performance.” (2015). <[http://www.edmundoptics.com/technical-](http://www.edmundoptics.com/technical-resources-center/imaging/wavelength-effects-on-performance/)
1133 [resources-center/imaging/wavelength-effects-on-performance/](http://www.edmundoptics.com/technical-resources-center/imaging/wavelength-effects-on-performance/)> (Jul. 14, 2015).

1134 Weber-Shirk, M. L. (2008). “An automated method for testing process parameters.”
1135 <<http://confluence.cornell.edu/display/AGUACLARA/Process+Controller+Background>>
1136 (Jul. 4, 2015).

1137 Wei, N., Zhang, Z., Liu, D., Wu, Y., Wang, J., and Wang, Q. (2015). Coagulation behavior of
1138 polyaluminum chloride: Effects of pH and coagulant dosage. *Chinese J. Chem. Eng.*, 23(6),
1139 1041-1046.

- 1140 Xiao, F., Lam, K. M., Li, X. L., Zhong, R. S., and Zhang, X. H. (2011). PIV characterization of
1141 flocculation dynamics and floc structure in water treatment. *Colloid. Surface. A.*, 379(1-3),
1142 27-35.
- 1143 Yao, M., Nan, J., and Chen, T. (2014). Effect of particle size distribution on turbidity under
1144 various water quality levels during flocculation processes. *Desalination*, 354, 116-124.
- 1145 Zhang, Z., Zhao, J., Xia, S., Liu, C., and Kang, X. (2007). Particle size distribution and removal
1146 by a chemical-biological flocculation process. *J. Environ. Sci.*, 19(5), 559-563.